Engineered biochar derived from pyrolyzed waste tea as a carbon support for Fe-N-C electrocatalysts for the oxygen reduction reaction

(Article begins on next page)

20 March 2024

Engineered biochar derived from pyrolyzed waste tea as a carbon support for Fe-N-C electrocatalysts for the oxygen reduction reaction

Stefano Zago[1], Mattia Bartoli[2,3], Mohsin Muhyuddin[4], Giovanni M. Vanacore[4], Pravin Jagdale[2], Alberto Tagliaferro[1,3], Carlo Santoro[4], Stefania Specchia[1*]

[1] *Politecnico di Torino, Department of Applied Science and Technology, Corso Duca degli Abruzzi 24, 10129 Torino, Italy*

[2] *Istituto Italiano di Tecnologia, Center for Sustainable Future Technologies - CSFT@POLITO via Livorno 60, 10144 Torino, Italy*

[3] *Consorzio Interuniversitario Nazionale per la Scienza e Tecnologia dei Materiali (INSTM), Via G. Giusti 9, 50121 Firenze, Italy*

[4] *University of Milano-Bicocca, Department of Material Science, Building U5, Via Cozzi 55, 20125 Milano, Italy*

* Corresponding author: stefania.specchia@polito.it

Graphical Abstract
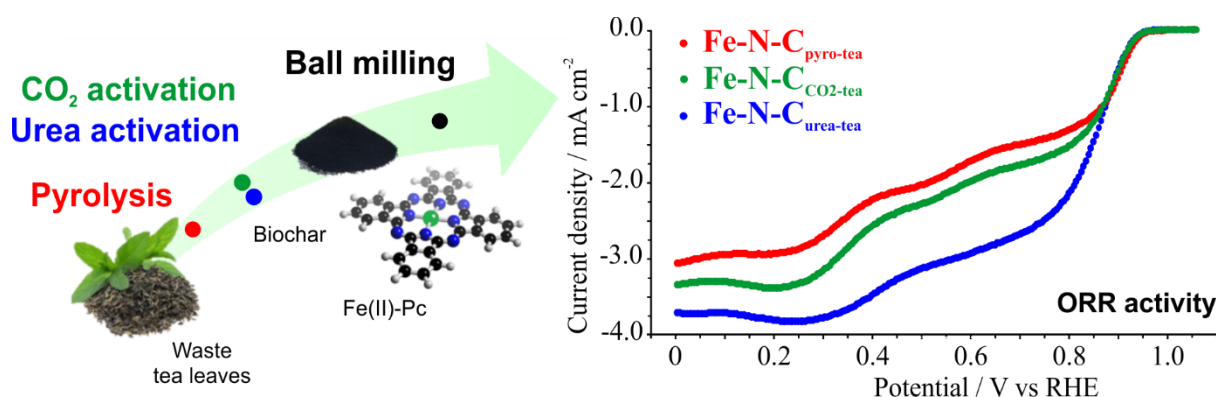
Highlights

- Biochar produced from pyrolyzed waste tea leaves and activated with CO_2 or urea

- Fe-N-C electrocatalysts obtained by ball milling of biochar and Fe phthalocyanine

- Good ORR activity in alkaline environment and methanol tolerance, high durability

1

- Correlation of the ORR activity with porosity, biochar's functionality, Fe amount

Keywords

Abstract

Platinum metal group (PGM-free) electrocatalysts for oxygen reduction reaction (ORR) were synthesized by ball milling of activated biochar and Fe(II) phthalocyanine. The biochar used as a carbon support was produced from pyrolysis of waste tea leaves at 1500 °C in argon atmosphere. The pyrolyzed waste tea was then activated with CO_2 or urea. FE-SEM, HR-TEM, XPS, and Raman analyses were performed to investigate the morphology and the physicochemical properties of the electrocatalysts. The ORR activity and methanol tolerance of the Fe-N-C electrocatalysts were tested in rotating ring disk electrode (RRDE), showing promising results in terms mass activity, onset and half-wave potential in alkaline environment. Two different short potential cycling protocols demonstrated the high stability of these Fe-N-C electrocatalysts, especially when compared with a 20 wt. % commercial Pt/C electrocatalyst.

1. Introduction

Fuel cells are clean and efficient energy devices able to harvest electric energy from the chemical reaction of a fuel and oxygen without any byproduct. For the commercial development of this technology it is extremely important to reach high values of activity and efficiency, because at the present time the cost is too high to successfully take on the market [1,2]. Up to now the most widely used electrocatalysts for the cathodic oxygen reduction reaction (ORR) in polymer electrolyte fuel cells (PEFC) make use of platinum or other noble metals to favor this sluggish reaction [3,4], but they face problems, such as expensive price, scarcity and geopolitical concerns correlated with the location

2

of the main producers [5]. It is also important to note that Pt-based electrocatalysts for ORR suffer easy carbon corrosion and Pt particle aggregation [6], meaning poor long-term stability. Moreover, Pt-based electrocatalysts are highly reactive towards alcohols, representing a drawback for direct alcohol fuel cells (direct methanol and ethanol fuel cells, DMFC/DEFC) because of the so-called methanol (or ethanol) crossover effect [7,8]. This phenomenon involves the diffusion and electro-osmosis of the alcohol through the electrolyte membrane from anode to cathode (considering convective transport of the alcohol negligible). With noble metal electrocatalysts at the cathode, the crossing over flowing fuel undergo instant oxidation with a consequent presence of a mixed-potential at cathode, which causes considerable voltage losses [9,10].

Through the ORR, oxygen is converted into water in a complex multielectron transfer process. The mechanism is still unclear and under debate, although various models have been developed. The generally accepted model by Wroblowa [11] simplifies the steps into two main pathways which are the four-electron process and the two-electrons two-steps process with the peroxide intermediate. Although it has been reported by kinetic studies that the favored pathway is the one with the peroxide intermediate, this is not desired in fuel cells because it negatively affects the stability of electrode and membranes. Therefore, the best electrocatalysts are those able to privilege the desired four-electron mechanism [3].

Great efforts are being made in the design and development of low cost and more stable ORR electrocatalysts not containing platinum group metals (PGM) but still retaining a good activity in alkaline or acidic environment [12–14]. Obtaining such a durable and efficient electrocatalyst would lead to both decreased Pt usage and lower production cost of PEFC because of the industrial scalability [15–17]. In the last decades the usage of transition metals or even metal-free electrocatalysts have been proposed. They can reach electrocatalytic activities similar to those of PGM exploiting a process of heteroatom doping (mainly nitrogen-doped catalyst), although the mechanism of reaction and active centers are still object of debate [18,19]. In Fe-N-C type PGM-free

electrocatalysts, the most studied in the literature, the presence of iron in the catalyst have been suggested to enhance the activity thanks to a multitude of active sites all able to catalyze the ORR. For these materials, both metal and metal-free sites have been characterized comparing their selectivity towards 4 electrons and 2+2 electrons process. The types of nitrogen and iron−nitrogen functionalities studied mainly consist of in-plane defects, such as graphitic nitrogen and Fe coordinated to 3 or 4 N atoms, as well as different edge sites such as pyridinic-, pyrrolic-, quaternary-N and Fe-N_x sites [13,20]. Some authors imply a direct responsibility of nitrogen functionalities in carbon support for ORR activity, while others suggest that nitrogen only acts as a coordinating environment for metal ions and these are the actual reactive centers. Integration of Fe-N_x sites in a π-conjugate carbon plane, like graphite or graphene, allows modification of electron donating and withdrawing capability of the carbon layer, thus improving the ORR activity [21,22].

Up to now, in acidic environment noble metals still shows the best activity performance, but in alkaline environment PGM-free electrocatalysts are becoming relevant because of the particular mechanism that takes place, achieving high electrocatalytic activity even without platinum or other precious metals. The anion exchange membrane fuel cells (AEMFCs) are attracting a lot of interest and their current development is described in a good number of reviews [3,23,24]. The study of N-doped porous carbon materials has become an interesting topic because of their low cost, non-toxicity and renewability, displaying a promising performance as metal-free and metal-doped ORR electrocatalysts [14,25]. A specific niche is being taken by biomass-derived material, especially from wastes, that have been considered for supercapacitors, metal-air battery, and fuel cells applications [26–29]. The already low cost of PGM-free materials is even lowered if the starting precursors are a common and abundant waste. Moreover, this pathway of valorizing waste into valuable resources and products fits very well in the view of circularity [30,31]. Other than that, the synthesis of PGM-free electrocatalysts from waste biomass is usually very simple and straightforward involving mainly pyrolysis and wet impregnation or grinding. Recently reported biomass derived materials with good

activity were obtained from coconuts shells [32], eggplants [33], soy beans [34], or other biomass sources [35], but they are only the tip of the iceberg, as a multitude of materials have been synthesized, sometimes with more provocative value than real scientific interest [36,37]. Furthermore, very recently waste biomass and waste face surgical masks have been recycled to produce bio-char and Fe-based catalysts as waste valorization from the pandemic caused by the virus SARS-CoV-2, with interesting catalytic activity towards ORR [38,39]. In short, there is still room to improve because of the extremely high requirements set for the fuel cell technology [15], but the approach of turning waste into wealth, reducing pollution and obtaining green energy is nowadays not only accepted but also required in the view of sustainability of products and reduction of wastes [40,41].

Previous works from our group included Fe-N-C type PGM-free electrocatalysts, obtained by heat treatment of iron phthalocyanine with commercial or home-made carbon supports [42–44]. For this work, the novelties are in (i) the synthesis of the carbon support from a waste biomass, specifically spent tea leaves, and (ii) the use of ball milling instead of heat treatment for iron integration into the carbon matrix. Ball milling exceeds manual grinding as it allows the tuning of various parameters in the synthesis, such as rotation rate and time, relative ratio between precursors [45]. It is worth noting that ball milling process is a mechano-chemical technique capable of producing localized hot spots reaching temperatures that exceed 600 °C [46–49]. Purpose of this study is the engineering of the biomass carbon structure and incorporation of iron active sites in the material with ball milling method. The starting biomass material, pyrolyzed spent tea leaves, presents a macro-porous structure. Hence, we increased the porous network by activation with CO_2 or urea in order to artificially create (and eventually, tune) the pores. Tea is a very common waste commonly used by many families as a drink for breakfast or afternoon break. This implies that there are lots of factories producing tea beverages which have a spent product that normally is thrown away without being recycled or reutilized. Thus, this waste tea could find a second life as a carbon source to be a precursor for ORR electrocatalyst [50,51], under the concept of recycling and circular economy [52]. In order to ensure

the methodology can be applied to the most common available biomass, we used commercial tea bought from supermarket without requiring a specific variety.

2. Materials and methods

2.1 Materials

Commercial tea leaves were recovered after the preparation of the beverage. Prior to the pyrolysis, they were dried at 105 °C for 72 h. Urea ($CO(NH_2)_2$ > 99%), potassium hydroxide (KOH, 99.0% purity), ethanol ($CH_3CH_2OH \geq$ 99.8% purity), acetone (($CH_3)_2CO \geq$ 99.8% purity), Nafion® 5 wt.% hydro-alcoholic solution, and iron(II) phthalocyanine ($C_{32}H_{16}N_8Fe$, herein after named Fe-Pc, 90% purity) were purchased from Sigma-Aldrich. Ultrapure nitric acid (65% HNO_3) and hydrogen peroxide (30% H_2O_2) were purchased from Merck. Nitrogen, oxygen, and argon gases were supplied in cylinders by SIAD with 99.999% purity. Ultrapure deionized water obtained from a Millipore Milli-Q system (resistivity >18 MΩ cm) was used for the experiments. All reagents were used as received without further purification. With the purpose of comparison, 20 wt.% Pt/C (HiSPEC[TM] 3000, Pt 20 wt.% on carbon black, Johnson Matthey) was purchased from Alfa Aesar.

2.2 Methods

2.1. Biochar synthesis

Exhausted tea leaves (100 g) were pyrolyzed using a vertical furnace and a quartz reactor, heating rate of 15 C° min^{-1}, and kept at 400 °C for 30 min in a nitrogen atmosphere according to Noori et al. [53]. Then, a further thermal annealing was run accordingly with previous described procedures [54,55]. Tea-derived biochar was treated by using a vacuum electric furnace (Pro.Ba., Cambiano, Italy) in an argon atmosphere, at a controlled pressure of 550 mbar, using a heating rate of 150 °C h^{-1}. Once the target temperature (1500 °C) was reached, it was kept constant for 30 min. Subsequently,

the furnace was cooled at room temperature with the same thermal gradient used for heating. The so-produced tea-derived biochar was labelled $C_{pyro-tea}$.

Afterwards, a sample of $C_{pyro-tea}$ was mixed in a ceramic mortar with urea with a 1:1 weight ratio and placed into a pre-heated tubular furnace (Carbolite TZF 12/65/550), where it was kept at 800 °C for 30 min in argon atmosphere. The sample recovered was labelled $C_{urea-tea}$ and used without any further treatment.

Similarly, a sample of $C_{pyro-tea}$ was placed into a pre-heated in a tubular furnace (Carbolite TZF 12/65/550) and there kept at 800 °C for 30 min in CO_2 atmosphere (10 mL min^{-1}). The sample recovered was named $C_{CO2-tea}$ and used without any further treatment.

2.2. Catalysts synthesis

Three different Fe-N-C electrocatalysts were prepared via ball milling using pyrolyzed commercial tea and Fe-Pc as precursors, with the Fe-Pc as a unique source of either Fe and N. The Fe-N-C catalysts were obtained by high energy ball milling treatment using three stainless steel balls, each 8 mm in diameter, in a jar of 25 ml volume that vibrates at a frequency of 20 Hz for 99 minutes in a translational Mixer Mill MM 400 by Retsch. We introduced in the jar a 1:2 weight ratio mixture of Fe-Pc and the carbon supports derived by the pyrolysis of tea, after verifying that this was the combination which provided the best results in terms of ORR onset potential. The electrocatalysts obtained were labelled Fe-N-$C_{pyro-tea}$, Fe-N-$C_{CO2-tea}$ and Fe-N-$C_{urea-tea}$, respectively. There was no further treatment for the electrocatalysts.

2.3. Electrocatalysts characterization – physical-chemical characterization

The morphology of the catalysts was investigated using a Field-Emission Scanning Electron microscope (FE-SEM, Zeis SupraTM 40) equipped with an energy dispersive X-Ray analyzer (EDX, Oxford Inca Energy450).

High-Resolution Transmission Electron Microscopy (HR-TEM) investigations were performed at the Microscopy Platform of the University of Milano-Bicocca (Italy) using a JEOL JEM 2100P operating at 200 kV, equipped with a LaB6 source, and exhibiting a nominal point resolution of 2.4 Å. The synthesized samples were dispersed in a solvent and transferred via drop casting onto a Cu grid, covered with a thin (3-4 nm) amorphous Carbon membrane. HR-TEM images were recorded with a Gatan RIO CMOS camera and taken at room temperature at different magnifications, with the TEM operated in bright-field parallel imaging mode, and adopting an in-gap objective aperture. Chemical analysis was performed using an Oxford Energy Dispersive X-Ray (EDX) detector while the microscope was operated in Bright-Field (BF) and High Angle Annular Dark-Field (HAADF) Scanning TEM (STEM) mode.

XPS spectra were recorded by using a PHI 50 0 0 Versaprobe (Physical Electronics, Chanhassen, MN, USA) scanning X-ray photoelectron spectrometer (monochromatic Al K-alpha X-ray source with 1486.6 eV energy, 15 kV voltage, and 1 mA anode current). Origin software was used to deconvolute the narrow spectra and determine the relative Fe-, N-, O-, and C-type atomic composition, using Gauss line shape with a Shirley background.

Raman spectra were collected using a Renishaw inVia (H43662 model, Gloucestershire, UK) equipped with a green laser line (514 nm) with a 50× objective. Raman spectra were recorded in the range from 250 to 3,500 cm^{-1}.

XRD of powdered samples was conducted using Rigaku Miniflex 600 equipped with a copper source. Analysis was performed in the 2θ range of 10-90° with a step of 0.020° while the scanning speed was 1.000 °/min.

The specific surface area of the samples was measured by means of N_2 adsorption/desorption at −196 °C on a Micrometrics ASAP 2020 Plus version 1.03 instrument (Micromeritics Instrument Corporation, USA). Before the analysis, the samples were degassed under vacuum for 3 h at 150 °C. The Brunauer–Emmett–Teller (BET) model was applied for data analysis. The volume of the

micropores, along with the differential surface area distribution, was obtained using a Non-Local Density Functional Theory (NLDFT) model calculation included in the Micromeritics instrument software.

The iron weight percentage in the Fe-N-C electrocatalysts was determined by inductively coupled plasma optical emission spectroscopy (ICP-OES) with a ICP-OES Optima 7000 DV PerkinElmer instrument. Prior to analysis, 20 mg of each powder were acidified in a 4 ml of HNO_3 and 1 ml of H_2O_2 and digested in two steps at 1000 W each, 20 + 30 min each (220 °C).

2.4. Electrocatalysts characterization – electrochemical characterization

The electrocatalysts were electrochemically characterized in a three electrode cells. The cell was equipped with a with (i) a glassy carbon disk (and platinum ring) working electrode (disk diameter 4 mm, ring outer and inner diameters 7 and 5 mm, respectively), which was mounted on a rotating disk electrode (RDE) equipment (model RRDE-3A ALS, Japan), (ii) a saturated calomel electrode (SCE) for RRDE measurements, or a saturated Ag/AgCl reference electrode for RDE durability measurements, (iii) a gold wire counter electrode. For the electrochemical tests, the potential of the working electrode was controlled by a potentiostat (Bio-Logic SP-150, France). The electrolyte was a 0.1 M KOH aqueous solution, pH = 13.

All measured potentials were corrected and converted to potential versus reversible hydrogen electrode (RHE) according to the following equation

$$E_{RHE} = E_{ref} + 0.059 \cdot pH + E_{ref}^0 \tag{1}$$

where E_{ref} is the measured working potential versus the reference electrode, E^0_{ref} is the potential of the reference electrode respect to the standard hydrogen electrode at 25 °C (0.197 V for Ag/AgCl, 0.241 V for SCE). All of the current densities were thus normalized per geometric area of the electrode.

The inks deposited onto the working electrode disk were prepared with a slightly modified version of a previously used method [42,43]. The inks were obtained by mixing 10 mg of electrocatalyst powder with 33 µl of Nafion 5 wt.% solution (achieving a 0.1456 ratio of mg Nafion / mg sample) and 750 µl of a mixture of water and ethanol in a 1:3 rate, resulting in a electrocatalyst density of in the ink equal to 0.0127 mg µl^{-1}. The ink was sonicated at 130 W for 30 min to achieve a good dispersion and 4 µl was pipetted on the glassy carbon electrode (area 0.1256 cm^2) obtaining an electrocatalyst loading on the electrode of 400 µg cm^{-2}. For the benchmarking tests using platinum, the amount of water-ethanol solutions was adjusted in order to reach a loading of 30 µg Pt cm^{-2} as suggested by the literature [56].

Before starting the tests, each electrocatalyst was subjected to 20 cyclic voltammetry (CV) between 0.0 and 1.2 V vs. RHE at 100 mV s^{-1} under N_2-saturated electrolyte to obtain a clean and stable catalyst surface. Then, a CV at 10 mV s^{-1} under N_2-saturated electrolyte was recorded.

Then, a first series of ORR steady-state polarization curves were measured performing a staircase voltammetry (SCV) with a potential step of 10 mV and a holding time of 30 s in O_2-saturated electrolyte, at room temperature. SCV measurement were used to optimize the amount of precursors to be used during the synthesis of the Fe-N-C electrocatalysts (in terms of maximum allowable amount of $C_{pyro-tea}$ and Fe-Pc in the jar for the ball milling, and relative ratio between carbon and iron).

Furthermore, on the optimized sets of electrocatalysts, the ORR polarization curves were measured performing a series of linear sweep voltammetry (LSV) at variable rotating speed of the RRDE (from 300 to 2,000 rpm). The electrolyte was purged with O_2 for at least 30 minutes before the experiments for facilitating the saturation of the liquid solution. The potential was scanned from 1.2 to 0 V vs RHE. For the evaluation of the hydrogen peroxide yields and the calculation of the number of electrons, the rotation speed of the electrode was set to 900 rpm, and the potential of the ring was fixed at 1.2 V vs RHE along with the experiments. The current generated by the disk (I_d) and by the

ring (I_r) were recorded, where the collection efficiency (N) was 38%. I_d and I_r were used to calculate the hydrogen peroxide produced (eq. 1) and the number of electrons transferred (n) (eq. 2) following the equations:

$$H_2O_2 = \frac{200 \cdot I_r/N}{I_d + I_r/N} \; [\%] \tag{2}$$

$$n = \frac{4 \cdot I_d}{I_d + I_r/N} \; [nr] \tag{3}$$

To quantify and compare the ORR activity we use two commonly used parameters, namely the onset potential (E_{on}), usually defined as the potential required to generate a current density of 0.1 mA cm^{-2} in a steady-state RDE experiment [57], and the half-wave potential ($E_{1/2}$), typically defined as the potential where half the maximum current density in the polarization curve is measured. As a term of comparison for ORR activity, we also used the mass activity of the electrocatalysts, calculated at 0.9 V vs RHE using the kinetic current J_k, to avoid the effects of the mass transport limitations [58]:

$$M.A. = -\frac{J_{k(0.9)}}{m_{cat}} \; [A \cdot g^{-1}] \tag{4}$$

$$J_{k(0.9)} = -\frac{J_{lim} \cdot J_{(0.9)}}{J_{lim} - J_{(0.9)}} \; [A \cdot cm^{-2}] \tag{5}$$

where m_{cat} is the electrocatalyst loading on the RDE, $J_{k(0.9)}$ is the mass transport-corrected current density at the selected voltage, J_{lim} is the diffusion limiting current density measured in the plateau region of the polarization curve at high overpotential, and $J_{(0.9)}$ is the measured current density at the selected voltage.

The methanol tolerance of the catalysts was evaluated in an O_2-saturated 0.1 KOH M solution, adding methanol to the solution from 0.001 to 2 M. LSV measurements were performed at each MeOH concentration, with an RDE speed of 900 rpm at 5 mV s^{-1} scan rate, room temperature.

A series of dynamic tests was performed to check the stability of the electrocatalyst to potential cycling. The tests followed two different protocols derived from a test proposed during the Fuel Cell

Commercialization Conference of Japan (FCCCJ) in 2011 [59], one involving a repeated cycling between 0.4 and 1.0 V vs. RHE (scan rate 500 mV s^{-1}) and the other involving repeated cycling between 0.4 and 1.0 V vs. RHE with a faster scan rate (1,000 mVs^{-1}) and 3 s hold at these two potentials. The cycling was performed under O_2-saturated electrolyte conditions [60], instead of N_2-saturated electrolyte conditions [59]. ORR steady-state polarization curves were recorded at the beginning of the test, after 1,500 cycles, and at the end of the test (4,500 cycles) to monitor the degradation of the activity of the electrocatalysts, performing a staircase voltammetry (SV) with a potential step of 10 mV and a holding time of 30 s in O_2-saturated electrolyte, at room temperature.

A third protocol to evaluate the stability of the electrocatalysts was performed through a chronoamperometry test performed in an O_2-saturated 0.1 KOH M solution keeping the potential fixed at 0.6 V vs RHE for 5,000 seconds.

3. Results

3.1 Materials physical-chemical characterization

The pristine tea-derived biochar was treated at high temperature to increase the conductivity, as shown by several works [61–64]. As reported by Tagliaferro et al. [55], biochar undergoes a structural reorganization process for temperature up to 1000 °C displaying a good crystallinity and graphitic domains size after an annealing at 1500 °C. Nonetheless, at that temperature it was observed a drastically reduction of the specific surface area, surface functionalities and pore volumes [65]. Accordingly, we enforced two different procedures able to enhance the specific surface area and nitrogen functionalities on our $C_{pyro-tea}$. Firstly, we treated the biochar with CO_2 promoting a physical activation and simultaneous introduction of oxygenated functionalities [66]. The other one was based on the thermal decomposition of urea leading to nitrogen doping and a simultaneous surface area increasing as consequence of a chemical activation [67].

A preliminary investigation of the morphology and composition of the pristine biochar, used as the carbon precursor of the electrocatalysts, and of the prepared electrocatalysts was run through FE-SEM and EDX analysis as shown in **Figure 1** and **Table 1**, respectively.
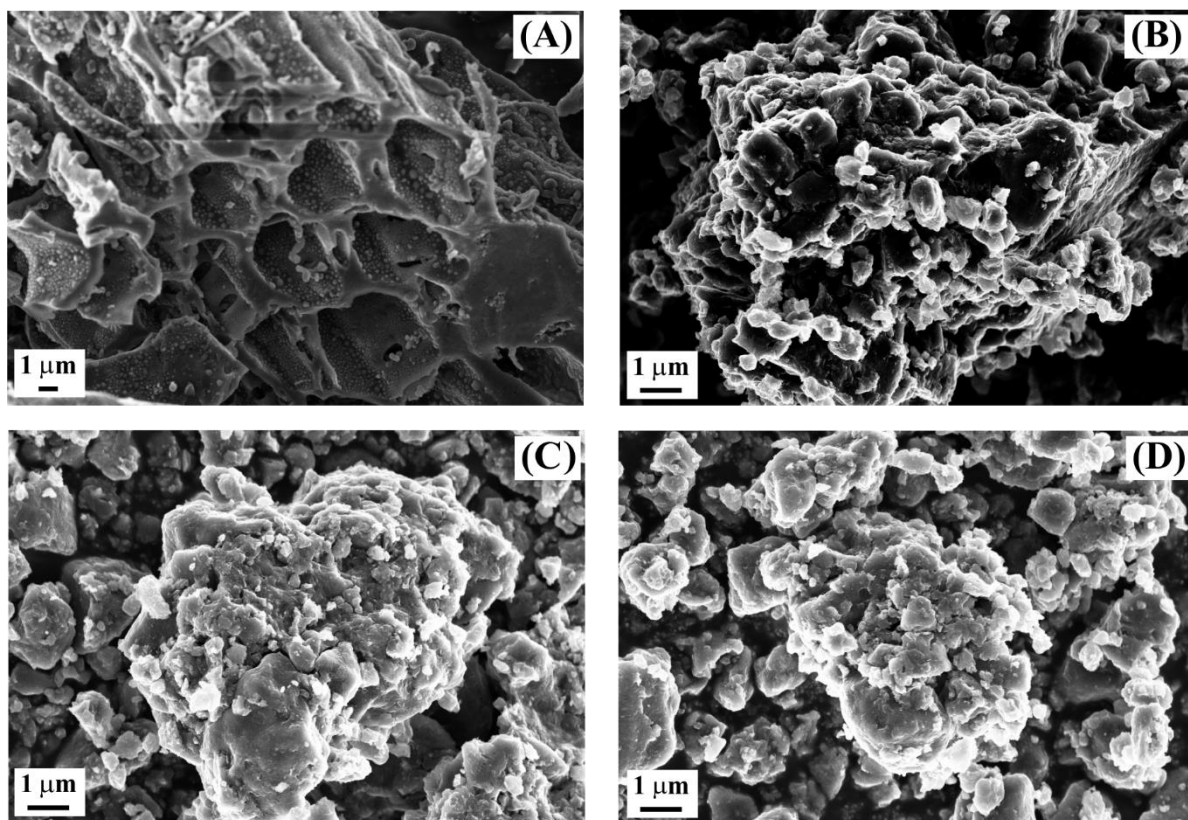

Figure 1. FE-SEM captures of $C_{pyro-tea}$ (A), Fe-N-$C_{pyro-tea}$ (B), Fe-N-$C_{CO2-tea}$ (C) and Fe-N-$C_{urea-tea}$ (D).

Table 1: Elemental composition by weight obtained by EDX analysis of pristine tea-derived biochar ($C_{pyro-tea}$), and the Fe-N-C electrocatalysts synthesized (n.d.: not detected). ICP-OES used to determine Fe on Fe-N-C electrocatalysts (last raw of the table).

Element	Sample			
[wt.%]	$C_{pyro-tea}$	Fe-N-$C_{pyro-tea}$	Fe-N-$C_{CO2-tea}$	Fe-N-$C_{urea-tea}$
C	83.5	67.8	69.4	74.3

O	6.2	17.9	21.8	17.7
Al	0.6	0.6	0.4	0.6
Si	0.2	0.5	0.3	0.3
P	0.5	0.4	1.3	n.d.
K	6.1	2.7	0.8	1.3
Ca	2.0	1.8	0.8	0.9
Na	0.6	0.	0.4	n.d.
Fe	n.d.	8.3	5.3	4.9
Fe*	-	3.59	3.81	2.59

*Fe measured by ICP-OES

The FE-SEM capture of $C_{pyro\text{-}tea}$ showed a material that bears reminiscence of the biomass original structure, even if channel walls appear mostly collapsed because of the high temperature reached during the pyrolysis. The ball milling induced a general homogenization of the morphology with the complete loss of the channeled structure [68]. This was most probably due to the mechanical disruption induced by ball milling. In fact, no appreciable differences are visible among the three Fe-N-C samples. This procedure was also able to insert the iron into the carbonaceous structure as shown by EDX analysis. Iron content rose up to over 8 wt.% in the Fe-N-C$_{pyro\text{-}tea}$, while in both Fe-N-C$_{CO2\text{-}tea}$ and Fe-N-C$_{urea\text{-}tea}$ it is close to 5 wt.%. Interestingly, Fe-N-C$_{urea\text{-}tea}$ showed the highest carbon content among the catalyst prepared, suggesting that urea decomposition removed other nitrogen heteroatomic doping elements. Slightly lower Fe content was identified using ICP-OES technique (**Table 1**).

A significant insight into the chemical structure of the electrocatalysts prepared was provided by XPS analysis, as shown in **Figure 2**. **Figure S1** and **Table S1** in the *Supporting Info* depicts the XPS survey spectra and main elements peak binding energies and relative areas of the samples examined.
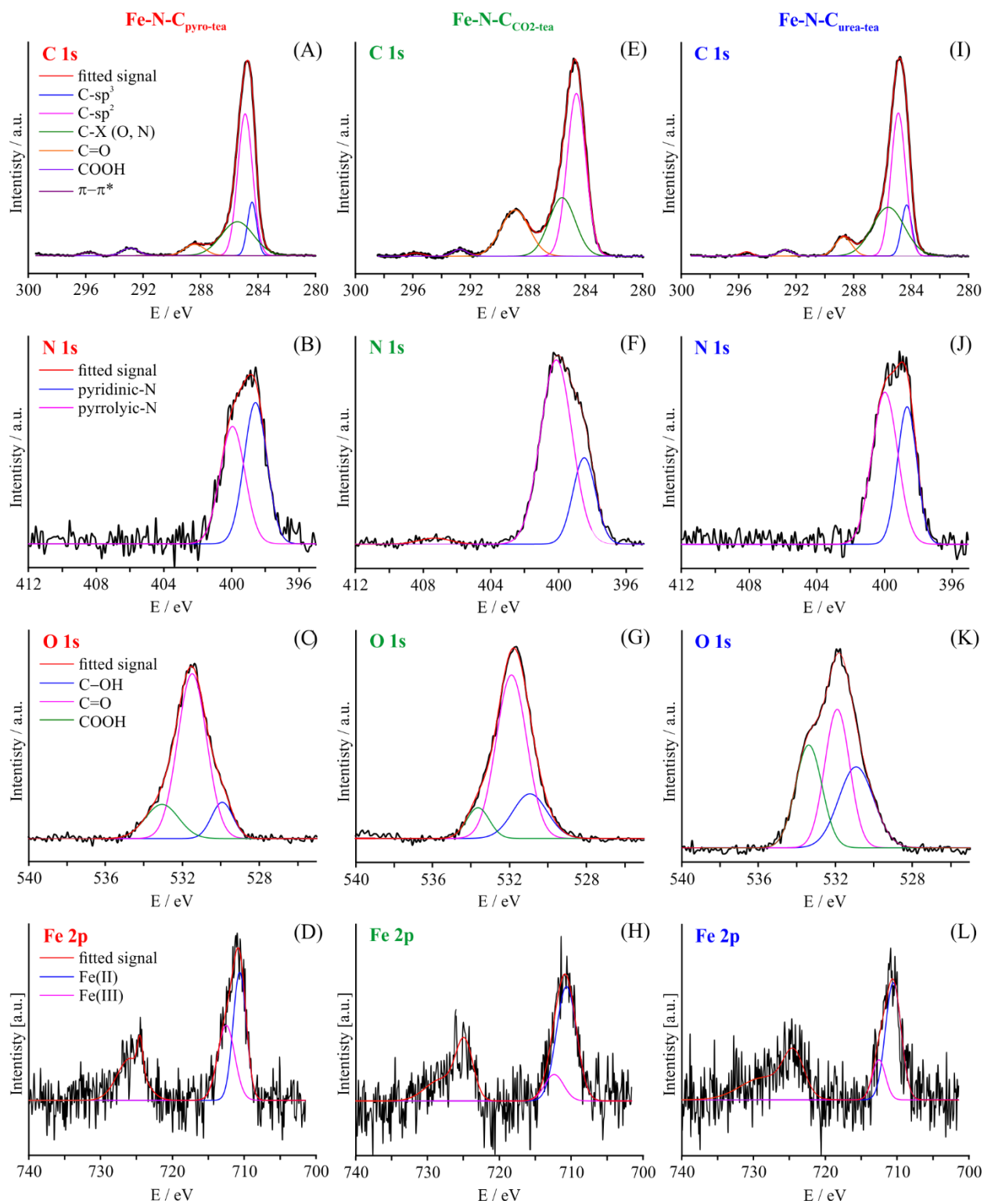
Figure 2. XPS high-resolution carbon, nitrogen, oxygen and iron spectra of Fe-N-C$_{pyro-tea}$ (A/B/C/D); Fe-N-C$_{CO2-tea}$ (E/F/G/H), and Fe-N-C$_{urea-tea}$ (I/J/K/L).

From the analysis of the C 1s spectra, it is possible to appreciate the presence of sp^3 carbon (around 284.2 eV) in Fe-N-C$_{pyro-tea}$ and Fe-N-C$_{urea-tea}$, while it is not present in the Fe-N-C$_{CO2-tea}$. This result supports the reaction pathway involved in the physical activation promoted by CO_2 [69] that depletes the non-graphitic carbon. The insertion of carbonyl residues into the graphitic carbon structure is witnessed by the presence of the peak at around 285.6 eV. Nitrogen signal displays two components due to pyridinic (around to 398.7 eV) and pyrrolic (around 400.1 eV) species. Fe-N-C$_{pyro-tea}$ and Fe-N-C$_{CO2-tea}$ show a ratio of pyridinic/pyrrolic nitrogen of 0.6 and 0.3, respectively, while Fe-N-C$_{urea-tea}$ is characterized by a higher ratio, close to 1.1. This is most probably due to the amine group inserted during the process, which evolved into high stable aromatic nitrogen such as pyridinic species. Interestingly, iron appears as both Fe(II) and Fe(III), reasonably as a consequence of a partial oxidation of original iron specie. Fe-N-C$_{pyro-tea}$ shows the lowest oxygen, content up to 55 %, while Fe-N-C$_{CO2-tea}$ shows the higher one with an amount of up to 78 %, and Fe-N-C$_{urea-tea}$ reaches a value of up to 68%. The lower stabilization of Fe(II) in Fe-N-C$_{urea-tea}$ compared with Fe-N-C$_{CO2-tea}$ is reasonably due to the random distribution of pyridinic nitrogen insert during the urea decomposition that probably does not reach the appropriate geometrical configuration for the stabilization of the iron center, while carbonyl residues in Fe-N-C$_{CO2-tea}$ can create more stable complexes.

Raman spectra reported in **Figure S2** of the *Supporting Info* show a disorganization of the materials after ball milling with the notable exception of Fe-N-C$_{urea-tea}$. In fact, Fe-N-C$_{urea-tea}$ shows a *I_D/I_G* value of up to 0.9 while the pristine tea derived biochar shows a very close value of up to 0.8. This is reasonably due to the radical rich environment promoted by the decomposition of the urea, that induced a further enlargement of crystalline domains.

Finally, we measured the specific surface area of the three electrocatalysts, as reported in **Table 2**. The adsorption/desorption isotherms are of Type II, according to the IUPAC classification [70], typical of non-porous or macro-porous materials. Fe-N-C$_{pyro-tea}$ has a very limited specific surface area, with few meso-pores and mostly macro-pores. With the activation treatment of the C$_{pyro-tea}$ with

CO_2 or urea, the materials display minimum values of the specific surface values not overcoming 32 $m^2\ g^{-1}$. The electrocatalysts are rather mesoporous, with relatively low micro-porosity according to the NLDFT model (carbon slit-shaped pores), as visible from **Figure S3** in the *Supporting Info*.

Table 2: Specific surface area and pore volume of the materials prepared (n.d.: not detected).

Support	Specific surface area [m² g⁻¹]	Micropores area [%]	Mesopores area %]	Total pore volume [cm³ g⁻¹]	Micropore volume [%]	Mesopore volume [%]
Fe-N-C$_{pyro-tea}$	1.0± 0.3	0.0	61.0	0.015	0.0	23.3
Fe-N-C$_{CO2-tea}$	24.3 ± 0.4	25.4	70.9	0.048	5.4	50.9
Fe-N-C$_{urea-tea}$	31.7± 1.9	18.0	80.4	0.036	5.7	70.6

3.2. Electrochemical characterization

3.2.1. RRDE tests

The activity of the Fe-N-C electrocatalysts synthetized from the various pyrolyzed tea leaves was tested in alkaline medium. Firstly, we tested the activity of the starting precursors of the Fe-N-C electrocatalysts, as shown in **Figure S4** of the *Supporting Info*. As expected, the C$_{pyro-tea}$ has practically no ORR activity, while the Fe-Pc has limited ORR activity. The synthesis procedure of the Fe-N-C electrocatalysts was optimized using the Fe-N-C$_{pyro-tea}$. Specifically, we noticed that putting the maximum allowable amount of C$_{pyro-tea}$ and Fe-Pc in the jar for the ball milling, 200 mg, the electrocatalyst obtained is more performing in terms of SCV, compared to using lower amount. **Figure S5** of the *Supporting Info* shows the higher activity obtained by starting with a batch of precursors of 200 and 150 mg. The ball milling time, 99 min, the maximum time allowed by the translational mixer, was selected without optimization, considering that a sufficiently long mixing

time should assure homogeneity in the final product, a high volumetric and specific capacitance, and enhanced ion-transportation within the pores. According to the literature [71–73], optimized time around 90-100 min assure a good degree of pulverization without losing porosity. Longer milling times, in fact, produce a reduction of micro-and meso-porosity. Lastly, we optimized the ratio of the precursors in terms of carbon-to-iron ratio to synthesize the Fe-N-C electrocatalysts. We tried three different $C_{pyro-tea}$ to Fe-Pc ratios (4:1; 3:1; 2:1), and the best option was the weight ratio 2:1 (see **Figure S6** of the *Supporting Info*). Thus, all the Fe-N-C electrocatalysts were synthesized by ball milling for 99 minutes, 200 mg precursors in the jar, in the weight ratio $C_{pyro-tea}$:Fe-Pc = 2:1.

Figure 3 shows the CV of the three best synthesized electrocatalysts in N_2-saturated alkaline electrolyte, after synthesis optimization. The similar shapes of the voltammograms confirm the similar electrochemical properties of the three electrocatalysts. The specific capacitance appears high for all the electrocatalysts, with the capacitive current values slightly higher for the Fe-N-$C_{CO2-tea}$. The activation of the biochar with CO_2 provided a electrocatalyst with a higher specific capacitance compared to the other materials. All the CV recorded show two pairs of peaks linked with the redox processes at around 0.33 V vs RHE and 0.82 V vs RHE for the Fe-N-$C_{CO2-tea}$ and Fe-N-$C_{CO2-urea}$., while the peaks of the Fe-N-$C_{pyro-tea}$ are at a slightly higher potential. These redox peaks values refer to the values of Fe(I)/(II) redox couple (0.25 V) and Fe(II)/(III) redox couple (0.8 V) of the Fe-Pc [74–76]. In fact, in these electrocatalysts, the peaks are clearly visible because the mixture biochar Fe-Pc is only ball milled, and not pyrolyzed (as most of the Fe-N-C electrocatalysts in the literature). This is reasonable considering the presence of both Fe(II) and Fe(III) in the electrocatalysts, as revealed by XPS analysis.
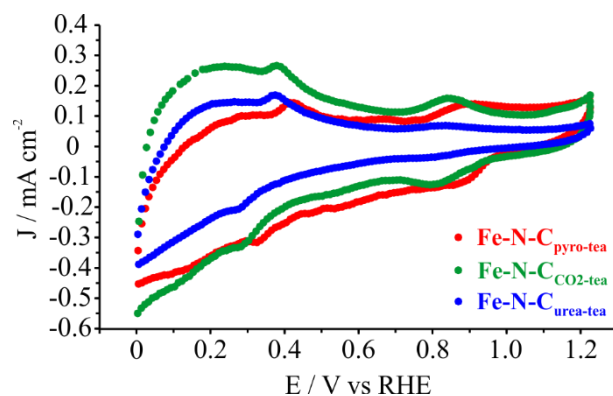
Figure 3. SCV curves of Fe-N-C$_{pyro\text{-}tea}$, Fe-N-C$_{CO2\text{-}tea}$, and Fe-N-C$_{urea\text{-}tea}$ recorded in RDE at room temperature, in N$_2$-saturated 0.1 M KOH solution, scan rate 10 mV s^{-1}, electrode loading 400 µg cm^{-2} (Pt/C: 30 µg$_{Pt}$ cm^{-2}).

Figure S7 of the *Supporting Info* shows the ORR activity results of the three Fe-N-C electrocatalysts from the LSV measurements, recorded at different rotation speeds of the RRDE. As expected, by increasing the rotational speed, the steady-state catalytic current density increases, due to a large increase of oxygen concentration on the electrode surface. The data collected at 900 rpm were extracted and compared with the ORR activity of the commercial 20 wt.% Pt/C (30 µg of Pt loaded on the electrode), as shown in **Figure 4**. While **Table 3** summarizes the calculated values in terms of mass activity, onset potential and half-wave potential.

According to these results, the performances of the three Fe-N-C electrocatalysts are similar terms of E_{onset} and $E_{1/2}$, but slightly higher for Fe-N-C$_{CO2\text{-}tea}$ in terms of mass activity, even if still far from the performance of Pt/C. The superior behavior of Fe-N-C$_{CO2\text{-}tea}$ is reasonably due to the morphological features and particularly to the slightly higher pore volume and a more ordered carbon structure. Interestingly, the CO$_2$ or urea activation that followed the starting pyrolysis of the tea leaves allowed to obtain two slightly more performing electrocatalysts compared with the Fe-N-C$_{pyro\text{-}tea}$. As a comparison with other biomass derived electrocatalysts from the literature, it is worth noting that a large number of electrocatalyst are reported and the vast majority of them falls in the range of 0.80-

1.00 V for the onset potential and 0.70-0.95 V for the half-wave potential, in 0.1 KOH electrolyte [26,27,29]. However, mass activity values are not reported in the literature. Also, acidic data are rarely presented as the activity for these materials tends to be much lower in low pH environment.
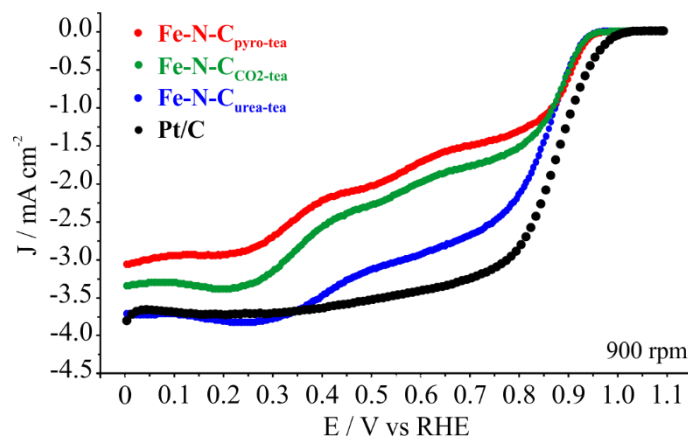

Figure 4. LSV curves at 900 rpm of Fe-N-C$_{pyro-tea}$, Fe-N-C$_{CO2-tea}$, and Fe-N-C$_{urea-tea}$ in comparison with a commercial 20 wt.% Pt/C, recorded in RDE at room temperature, in O_2-saturated 0.1 M KOH solution (scan rate 1 mV s^{-1}, electrode loading 400 μg cm^{-2}, 30 μg$_{Pt}$ cm^{-2} for Pt/C).

Table 3. Mass activity (M.A.), onset potential (E_{onset}) and half-wave potential ($E_{1/2}$) of the materials prepared related to the ORR measurements in **Figure 5**.

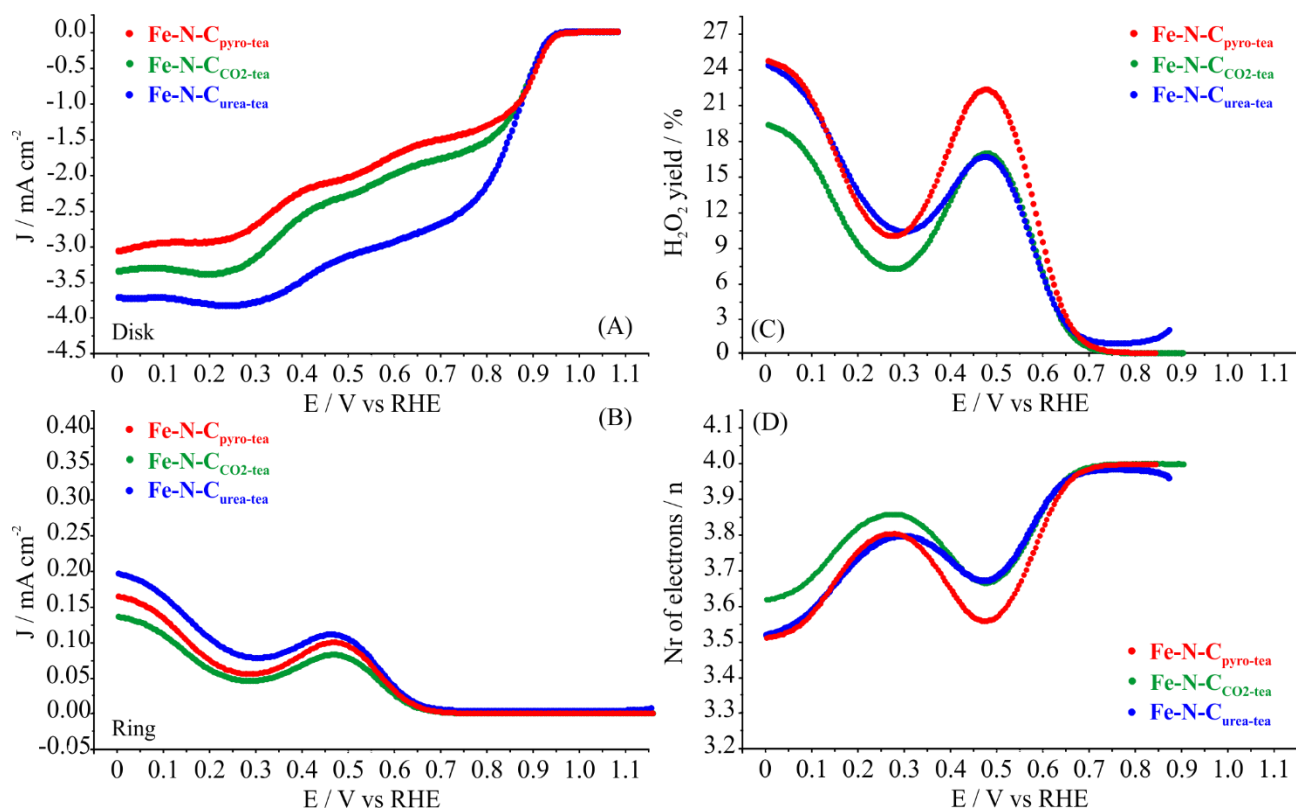|	Fe-N-C$_{pyro-tea}$	Fe-N-C$_{CO2-tea}$	Fe-N-C$_{urea-tea}$	20 wt% Pt/C
M.A. @ 0.9 V vs RHE [A g^{-1}]	2.32 ± 0.37	2.98 ± 0.24	2.31 ± 1.10	38.36 ± 9.24
E_{onset} **[V vs RHE]**	0.94 ± 0.01	0.95 ± 0.01	0.93 ± 0.01	0.99 ± 0.01
$E_{1/2}$ **[V vs RHE]**	0.89 ± 0.01	0.89 ± 0.01	0.87 ± 0.01	0.89 ± 0.01

Figure 5. RRDE measurements at 900 rpm of Fe-N-C$_{pyro-tea}$, Fe-N-C$_{CO2-tea}$, and Fe-N-C$_{urea-tea}$, recorded at room temperature, in O_2-saturated 0.1 M KOH solution (scan rate 1 mV s^{-1}, electrode loading 400 μg cm^{-2}). (A) Disk current density. (B) Ring current density. (C) Calculated hydrogen peroxide, ring potential fixed at 1.2 V vs RHE. (D) Calculated number of electrons transferred.

To better understand the ORR pathway and the selectivity of the reaction towards the production of H_2O_2 (partial 2 e$^-$ reduction), RRDE measurements at 900 rpm were performed on the three Fe-N-C electrocatalysts, as shown in **Figure 5**. Again, the best performance belongs to Fe-N-C$_{CO2-tea}$, producing less amount of H_2O_2 (not higher than 18%) compared to Fe-N-C$_{urea-tea}$ and Fe-N-C$_{pyro-tea}$ (**Fig 5C**). Clearly, the functionalization of the starting C$_{pyro-tea}$ with urea or CO$_2$ helps improving the selectivity of the electrocatalyst, even if the treatment with CO$_2$ seems to provide a slightly more selective electrocatalyst (average values of electron transferred for Fe-N-C$_{CO2-tea}$: 3.82), transferring

a higher number of electrons compared to Fe-N-C$_{\text{urea-tea}}$ (average values of electron transferred: 3.77)

and Fe-N-C$_{\text{pyro-tea}}$ (average values of electron transferred: 3.74, **Fig 5D**).

All of these considerations make the Fe-N-C$_{\text{CO2-tea}}$ electrocatalyst to be a good candidate for further

investigation on methanol tolerance and durability tests. For a better understanding, also Fe-N-C$_{\text{urea-tea}}$ electrocatalysts is considered for further analyses.

3.2.2. Methanol tolerance tests

The ORR performance of Fe-N-C$_{\text{urea-tea}}$ and Fe-N-C$_{\text{CO2-tea}}$ was tested for methanol tolerance in order

to evaluate the possible application of these catalysts in DMFC. As reported also in the literature,

usually the methanol tolerance of this class of Fe-N-C electrocatalysts is very good [43,77].

Consequently, they become good candidates to replace Pt as cathodic electrocatalyst for DMFC.

Figure 6 shows the polarization curves (LSV) of Fe-N-C$_{\text{urea-tea}}$ and Fe-N-C$_{\text{CO2-tea}}$ before and after the

addition of increasing concentrations of MeOH up to 2 M to the solution. The ORR activity is

practically unaffected by the presence of MeOH, with a limited shift of less than 10 mV of the onset

potential for both catalysts. Thus, the biomass derived electrocatalysts does not show a relevant

change in the shape and its loss of activity is negligible, especially if compared to the activity loss of

Pt/C (**Fig. 6C**). In fact, as a comparison, the commercial Pt/C electrocatalyst was also tested with the

same procedure, showing a collateral peak that starts to appear at concentrations of 0.1 M, and a shift

of the onset potential of more than 200 mV at concentration of 1 M, correlated with the preference of

the noble electrocatalyst for the methanol oxidation reaction. Thus, the biomass derived

electrocatalysts can be considered a valid alternative to mitigate the methanol crossover effect in
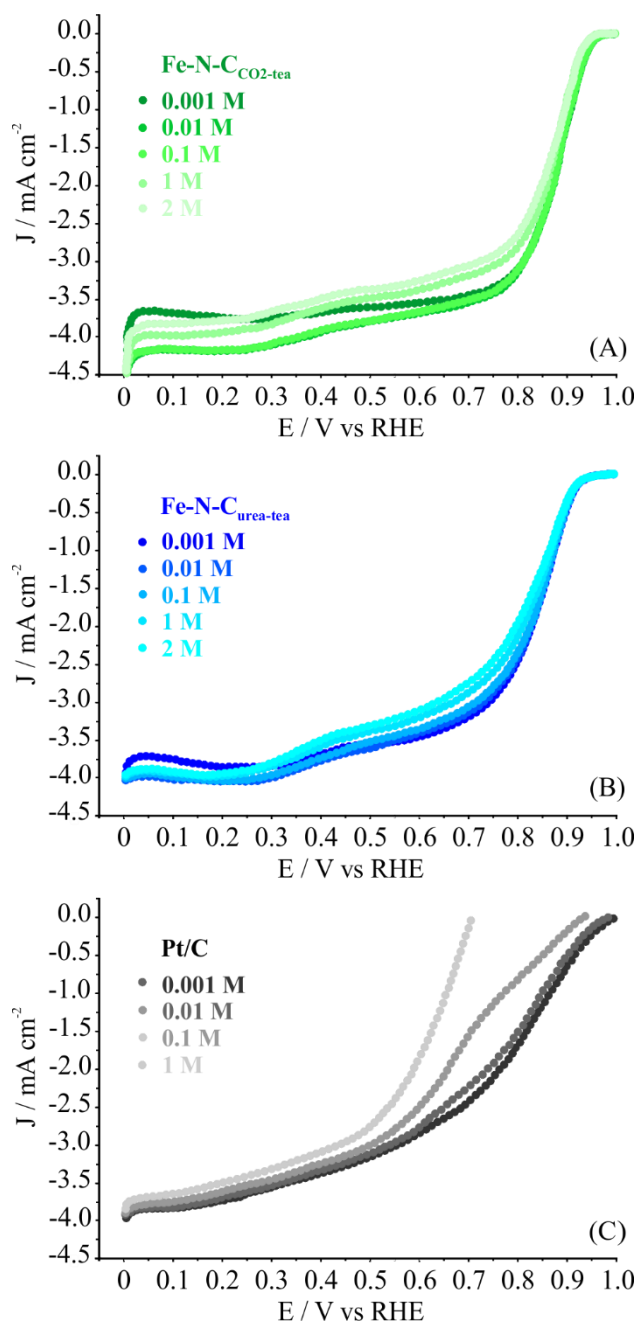
DMFC.

Figure 6. Methanol tolerance test: LSV plots at different methanol concentrations for Fe-N-C$_{CO2\text{-tea}}$ (A), Fe-N-C$_{urea\text{-tea}}$ (B), and Pt/C (C), in 0.1 KOH solution, saturated with O$_2$. Rotation speed 900 rpm, scan rate 5 mV s^{-1}, electrode loading 400 μg cm^{-2} (30 μg$_{Pt}$ cm^{-2} for Pt/C).

3.2.3. Durability and stability in RDE

The durability performance of the two most performing electrocatalysts was tested with two different protocols derived from a test proposed during the Japanese FCCCJ in 2011 [59], as shown in **Figures 7A/B**. The second protocol, with a faster scan rate and a 3 s hold at 0.4 and 1.0 V vs RHE, is supposed

to stress the material more, simulating the effective type of workload of a fuel cell and trying to evaluate the stress of months of usage with a test lasting a few hours. For sake of comparison, also the commercial Pt/C electrocatalyst was subjected to the same durability protocols.

Figures 7C-H and **Table 4** show the results of the potential cycling according to the two testing protocols. In terms of onset and half wave potential, there is practically no difference comparing the ORR activity at the beginning and end of the two durability protocols for Fe-N-C$_{urea-tea}$ and Fe-N-C$_{CO2-tea}$, while Pt/C lose almost 50 mV for both values. In terms of mass activity at 0.9 V vs RHE, Fe-N-C$_{urea-tea}$ displays no loss at all for both the protocols, while Fe-N-C$_{CO2-tea}$ lose 10% of mass activity after 4,500 cycles in the second protocol, while retaining its original activity without potential hold. These values indicate a good resistance to wide potential cycling for our waste tea derived electrocatalysts under a challenging O$_2$-containing environment, making the durability of this electrocatalyst interesting to be tested also in fuel cell in future works. Notably, the activity loss for Pt/C can reach over 80% in the most stressing condition, highlighting the well-known low durability of these electrocatalysts because of the carbon corrosion and Pt aggregation phenomena.

Chronoamperometric measurements were also employed to verify the stability of the electrocatalysts. **Figure S8** in the *Supporting Info* shows the results in terms of relative current density decay during 5,000 s at a constant potential of 0.60 V vs RHE in O$_2$-saturated 0.1 M KOH solution at room temperature. Fe-N-C$_{CO2-tea}$ resulted the most stable electrocatalyst, more than the commercial Pt/C, by retaining almost 94% of the current density (**Table 4**). This result could be explained considering the higher specific capacitance of this catalyst compared to that of Fe-N-C$_{urea-tea}$, as evident from **Figure 3**.
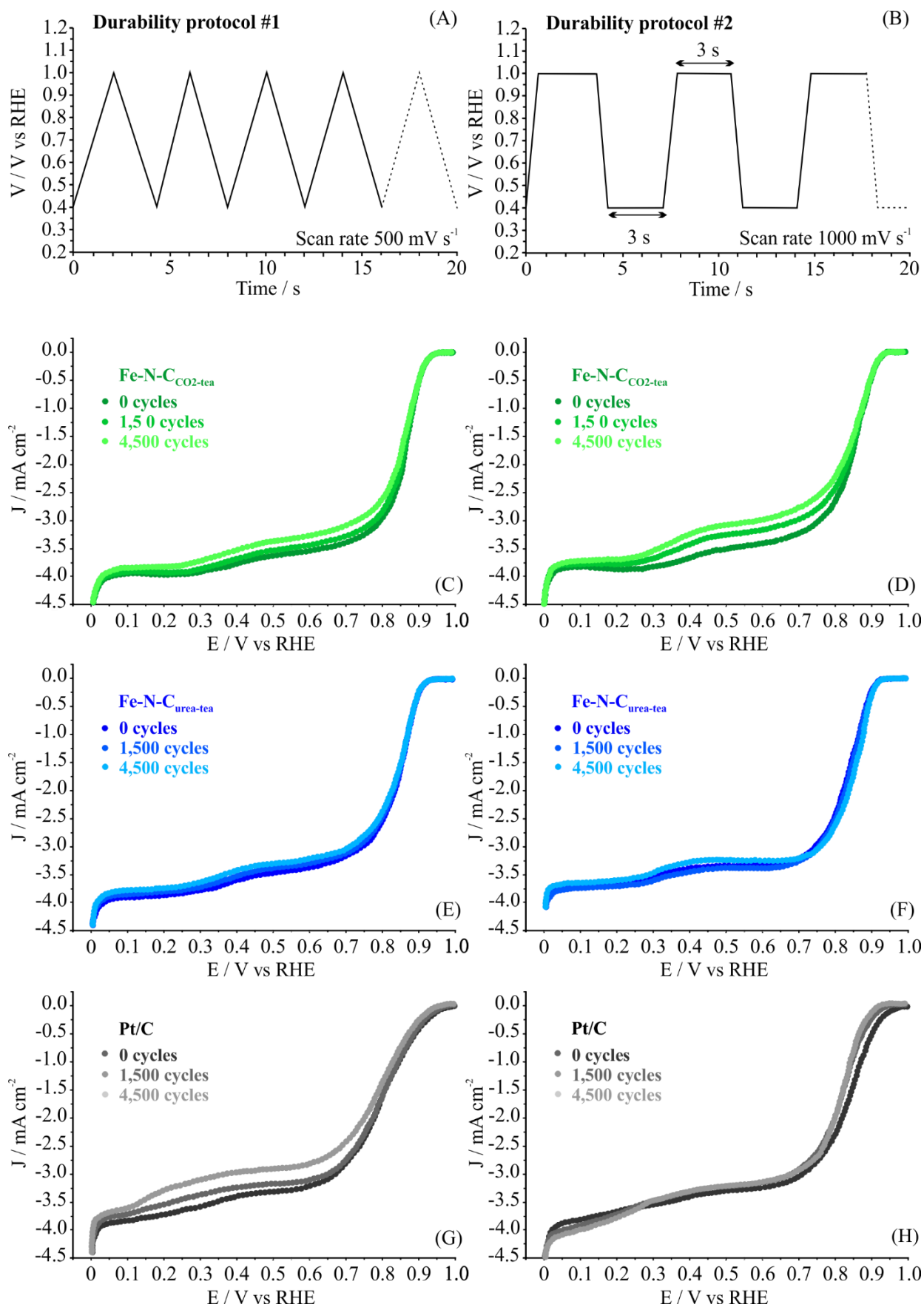
Figure 7. Schematic representation of the applied potential over time in the two durability protocols, performed in O_2-saturated 0.1 KOH electrolyte at room temperature (A/B). Durability protocols 1 (C/E/G) and 2 (D/F/G): LSV plots at different cycles for Fe-N-C$_{CO2\text{-tea}}$ (C/D), Fe-N-C$_{urea\text{-tea}}$ (E/F), and Pt/C (G/H), in 0.1 KOH solution, saturated with O_2. Rotation speed 900 rpm, scan rate 5 mV s^{-1}, electrode loading 400 μg cm^{-2} (30 μg$_{Pt}$ cm^{-2} for Pt/C).

Table 4. Mass activity loss calculated at 0.9 V vs RHE at the end of the two durability protocols and current density loss evaluated at the end of chronoamperometry at 0.6 V vs RHE.

	Fe-N-C$_{CO2\text{-tea}}$	Fe-N-C$_{urea\text{-tea}}$	20 wt% Pt/C
M.A. loss @ 0.9 V [A g^{-1}] **Protocol #1**	0	0	40%
M.A. loss @ 0.9 V [A g^{-1}] **Protocol #2**	10%	0	80%
C.D. loss @ 0.6 V [mA cm^{-2}] **Chronoamperometry**	6%	36%	19%

3.2.4. XRD, HR-TEM and STEM-EDX chemical analysis

Finally, to better understand the nature of these Fe-N-C electrocatalysts, and try to explain the better durability of Fe-N-C$_{CO2\text{-tea}}$, we performed also XRD (**Fig. S9** in the *Supplementary Info*) and HR-TEM and STEM-EDX measurements on Fe-N-C$_{CO2\text{-tea}}$ (**Figures 8 and 10**) and Fe-N-C$_{urea\text{-tea}}$ (**Figures 9 and 11**).

The diffraction spectra of both Fe-N-C$_{CO2-tea}$ (**Fig. S9A**) and Fe-N-C$_{urea-tea}$ (**Fig. S9B**) show a typical peak of disorganized carbon from 19° up to 30° 2θ with also a peak centered at 44.2°. This peak is composed by two components with the massively presence of a band centered at around 24.8° due to the sp^2 domains and one related to 002 reflection of graphite centered at 26.5° [61]. Fe-N-C$_{CO2-tea}$ showed a 44 % of graphitic component while Fe-N-C$_{urea-tea}$ reached up to 66%. Both samples showed an intense (100) reflection that was due a three dimensional crystal structure of the samples [78]. (100) reflection at 44.2° was far more intense in the case of Fe-N-C$_{CO2-tea}$ and far lower intense in Fe-N-C$_{urea-tea}$, suggesting a more graphitic-like structure of Fe-N-C$_{urea-tea}$, but more disordered. Furthermore, two peaks centered at 15.5° and 16.7° were both detected in Fe-N-C$_{urea-tea}$, due to the presence of Fe$_3$O$_4$ species, most probably formed during ball milling of Fe-Pc, as reported in the literature [79]. Fe-N-C$_{CO2-tea}$ showed only the band 15.5° and the other was probably too low in intensity to be appreciable. Anyhow, the proper assignation of the phase is not possible due to the super imposition of iron species signals with those of carbon. Nevertheless, it is reasonably supposing that the iron particles are formed by a combination of ferrites and iron (Fe(II) and (Fe(III) oxides, as also evident from XPS analysis (**Table S1** in the *Supplementary Info*). The complexity of the species and the simultaneous presence of carbon matrix prevents a unique assignation.

To better discern the assignation, we performed HR-TEM and STEM-EDX analyses on these two electrocatalysts. **Figure 8** shows HR-TEM images acquired in bright-field mode of the Fe-based nanoparticles in the graphitic matrix for the sample Fe-N-C$_{urea-tea}$. The particles exhibit a high-degree of crystallinity as evidenced by the well-defined atomic plane structure featured in the images. As shown in **Figures 8b-f**, we estimate a lattice plane distance of 0.34 nm, which agrees well with the lattice parameter along the (211) direction of the Fe$_3$O$_4$ lattice. This is consistent with XRD and XPS data, which show the presence of sharp peaks at 15.5° associated with a Fe$_3$O$_4$ phase.
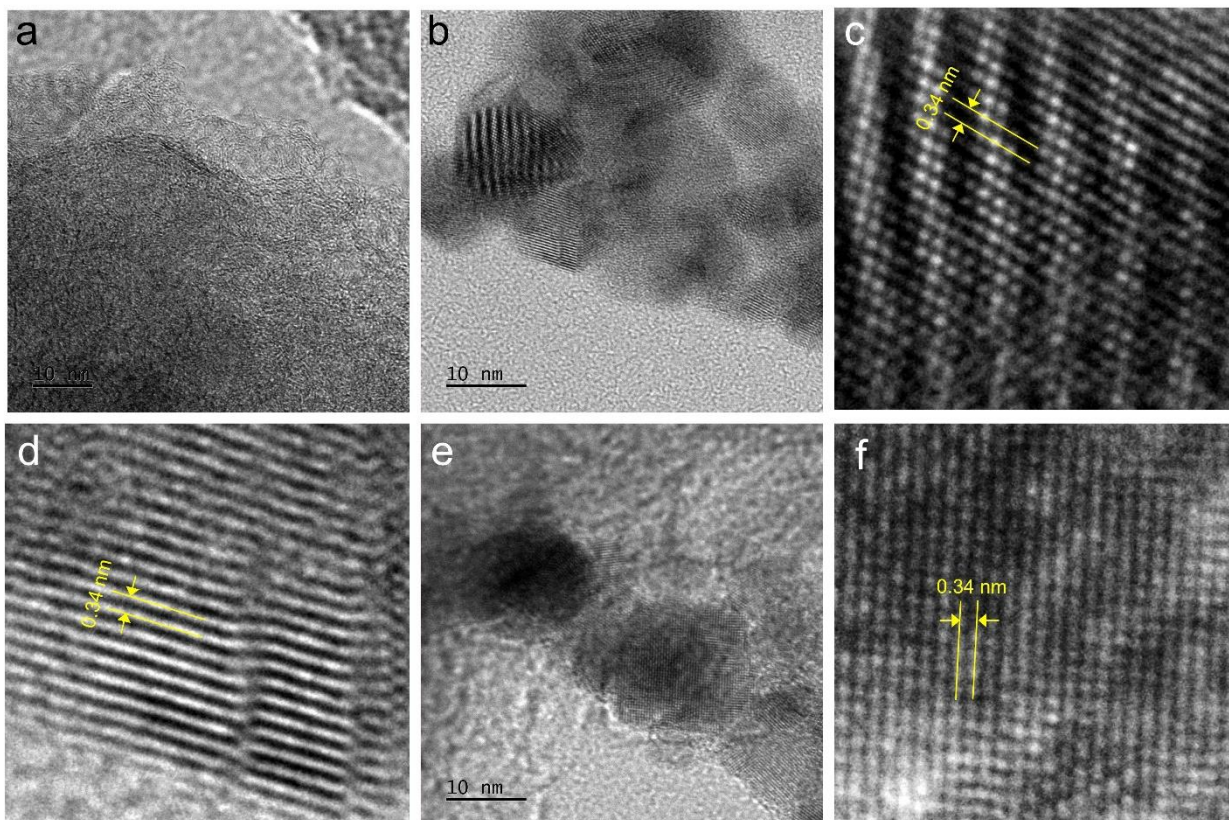
Figure 8. HR-TEM images acquired on sample Fe-N-C$_{urea-tea}$. (a): graphitic matrix; (b) and (e): Fe-based nanoparticles immersed in the graphitic matrix. (c) and (d): high magnification portion of the particles shown in panel (b). (f): high magnification portion of the particle shown in panel (e).

Figure 9 shows HR-TEM images acquired in bright-field mode of the Fe-based nanoparticles in the graphitic matrix for the sample Fe-N-C$_{CO2-tea}$. In this case, the particles seem to be much further incorporated into the graphitic matrix. Nevertheless, a certain degree of crystallinity is still visible (**Fig. 9c-d**) with a periodic atomic separation of 0.61 nm. The HR-TEM results are once again consistent with XRD and XPS data, which now observe a weaker contribution from the Fe$_3$O$_4$ phase.
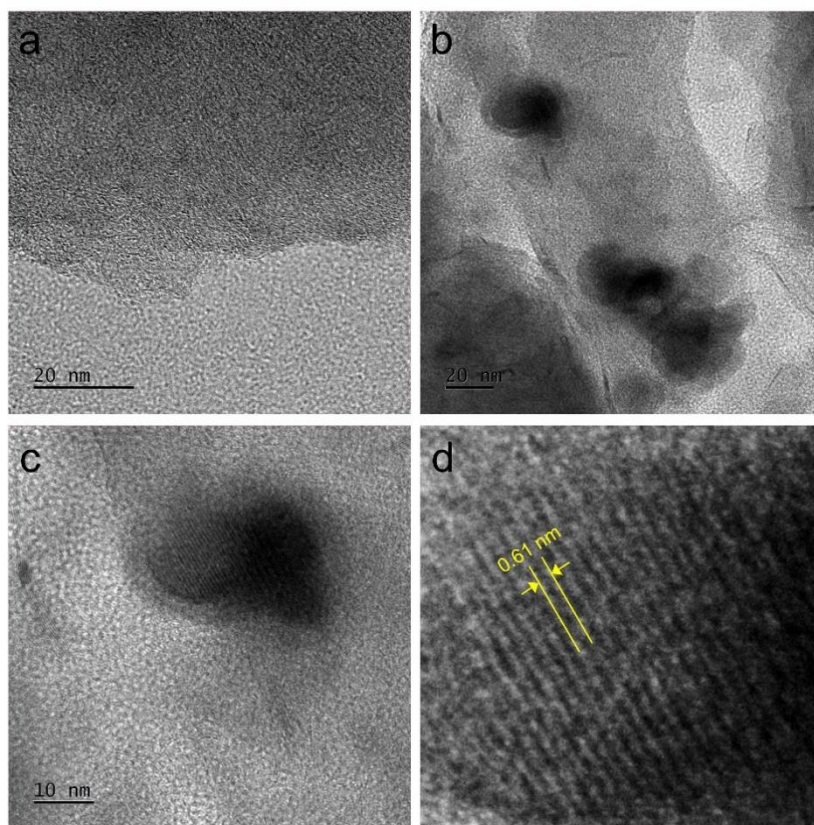
Figure 9. HR-TEM images acquired on sample Fe-N-C$_{CO2\text{-tea}}$. (a) graphitic matrix; (b and c) Fe-based nanoparticles immersed in the graphitic matrix; (d): high magnification portion of the particle shown in panel (c).

Figures 10 and **11** show STEM analysis of the investigated samples, together with EDX spectroscopy results for chemical mapping. In both cases of Fe-N-C$_{urea\text{-tea}}$ sample (**Fig. 10**) and Fe-N-C$_{CO2\text{-tea}}$ sample (**Fig. 11**), the nanoparticles appear darker in the BF-STEM images (**Figs. 10a** and **11a**), whereas they appear brighter in the DF-STEM images (**Fig. 10b** and **11b**). This is consistent with a higher atomic number with respect to the surrounding carbon matrix. As visible from the EDX chemical analysis (**Figs. 10d-f** and **11d-f**), accumulation of iron is observed at the nanoparticle sites, while carbon and oxygen are more homogeneously dispersed.
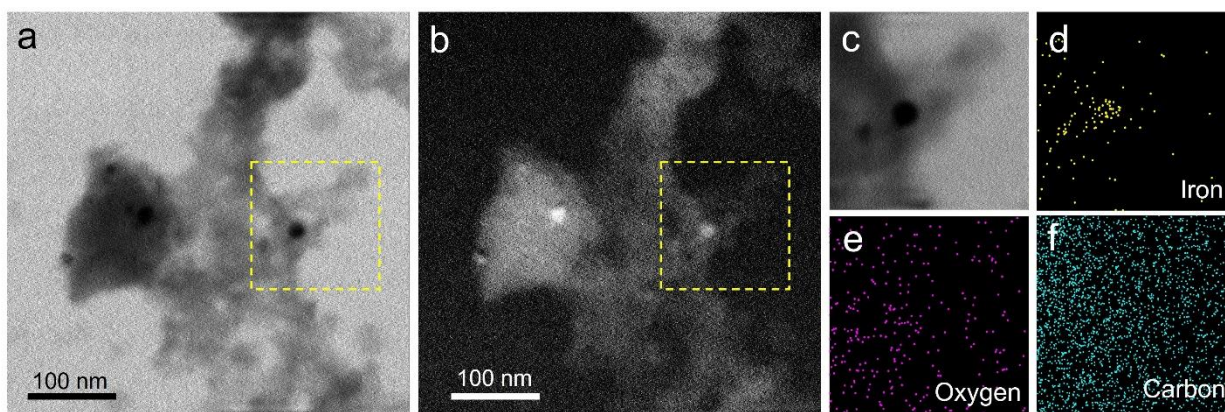
Figure 10. STEM-EDX analysis performed on the sample Fe-N-C$_{urea-tea}$. (a) BF-STEM image. (b) DF-STEM image. (c) BF-STEM image of the portion in panels a and b defined by the yellow square. (d)-(f) elemental area maps for iron (d), oxygen (e), and carbon (f).

Figure 11. STEM-EDX analysis performed on the sample Fe-N-C$_{CO2-tea}$. (a) BF-STEM image. (b) DF-STEM image. (c) BF-STEM image of the portion in panels a and b defined by the yellow square. (d)-(f) elemental area maps for iron (d), oxygen (e), and carbon (f).
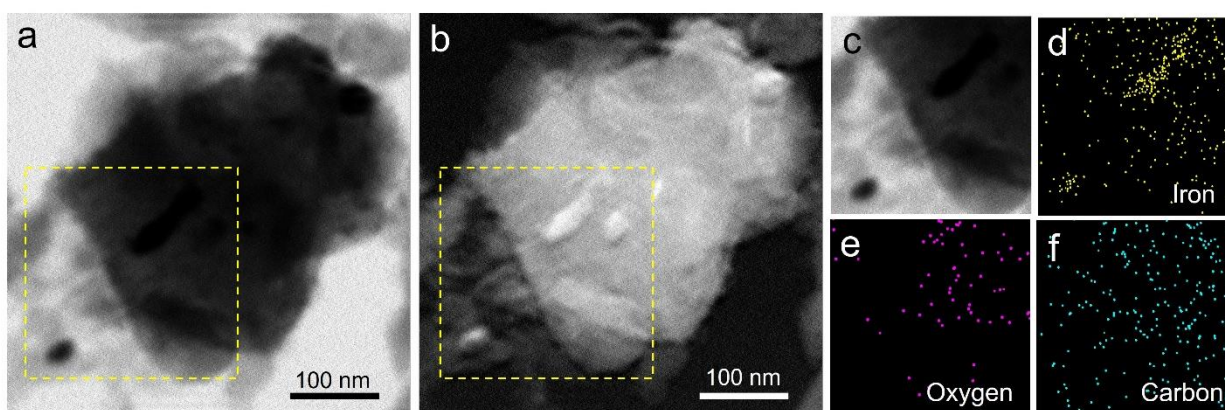
In summary, by combining the set of electrochemical measurements with the various morphological characterization (XPS, XRD, HR-TEM and ICP-OES), we can definitely rule out iron carbides and nitrides, and consider the main state of iron to be oxides. The slightly higher mass activity of Fe-N-C$_{CO2-tea}$ sample is consistent with the higher amount of Fe determined by ICP-OES (**Table 1**). Moreover, the higher incorporation level of Fe nanoparticles in the Fe-N-C$_{CO2-tea}$ sample appreciable

by HR-TEM (**Fig. 9**) can explain the better durability and stability of this catalyst when subjected to the two potential cycling protocols and chronoamperometry, as the iron sites are protected by the carbon scaffold, as also shown in the literature [80,81].

By concluding, the CO_2-activated biochar-derived Fe-N-C electrocatalyst can be considered a valid alternative to Pt/C based electrocatalysts, in particular for DMFC applications, thanks to the good stability, as also shown in the literature [17,80]. Activation of the biochar with CO_2 is necessary to enhance the selectivity of the final electrocatalyst towards the ORR via the 4-electrons pathway. We consider this work a starting point for a series of syntheses which could lead to useful electrocatalysts. In fact, thanks to the no cost of the starting precursor that is actually a waste, the pyrolysis of biomass could lead to low-cost electrocatalysts' synthesis, with benefits in terms of materials recycling and circularity [52]. The micro-porosity of the materials synthesized and the nitrogen content, to favor the formation of Fe-N_x active sites should be improved with further activation treatments and N-based doping of the biochar, to expect an enhanced ORR activity [14].

4. Conclusions

Three methanol tolerant and highly stable Fe-N-C electrocatalysts for ORR in alkaline environment were synthesized by ball milling Fe(II) phthalocyanine and biochar. The biochar was produced by pyrolyzing waste tea leaves in argon atmosphere at 1500 °C, followed by an activation with CO_2 or urea. The Fe-N-C electrocatalysts showed promising ORR activity in RDE and high methanol tolerance. In addition, the CO_2-activated biochar-derived Fe-N-C demonstrated to be very stable thanks to a higher degree of Fe oxides encapsulation into the graphitic carbon matrix. In fact, this electrocatalyst loses no more than 10% of the starting activity under potential cycling protocols. While a commercial 20 wt.% Pt/C electrocatalyst loses from 40 to 80% of its starting activity under potential cycling. Thus, the Fe-N-C$_{CO2-tea}$ electrocatalyst can be considered a valid alternative to Pt/C based electrocatalysts, in particular for DMFC applications. The results presented in this work

31

demonstrate that the use of biochar-derived materials in the synthesis of PGM-free Fe-N-C based electrocatalysts for ORR opens up possibilities in the design of alternative electrocatalysts. In fact, the proposed syntheses are quite straightforward and also easy to scale up or to be applied to other waste biomass materials, opening to the concept of biomass recycling and circular economy.

CRediT author statement

S.Z.: materials synthesis and electrochemical characterizations, data analysis, writing - original draft. M.B.: materials synthesis and physical-chemical characterizations, data analysis, writing - original draft. M.M.: electrochemical characterizations. P.J.: physical-chemical characterizations. G.M.V.: physical-chemical characterizations. A.T.: supervision, writing - review & editing, resources. C.S.: supervision, data analysis, review & editing, resources. S.S.: supervision, data analysis, writing - review & editing, resources.

Declaration of Competing Interest

The authors report no declarations of interest.

References

[1]   Y. Wang, K.S. Chen, J. Mishler, S.C. Cho, X.C. Adroher, A review of polymer electrolyte membrane fuel cells: Technology, applications, and needs on fundamental research, Appl. Energy. 88 (2011) 981–1007. https://doi.org/10.1016/j.apenergy.2010.09.030.

[2]   B.G. Pollet, S.S. Kocha, I. Staffell, Current status of automotive fuel cells for sustainable

        transport, Curr. Opin. Electrochem. 16 (2019) 90–95.

        https://doi.org/10.1016/j.coelec.2019.04.021.

[3]   N. Ramaswamy, S. Mukerjee, Fundamental mechanistic understanding of electrocatalysis of

        oxygen reduction on Pt and non-Pt surfaces: Acid versus alkaline media, Adv. Phys. Chem.

        2012 (2012). https://doi.org/10.1155/2012/491604.

[4]   M.K. Debe, Electrocatalyst approaches and challenges for automotive fuel cells, Nature. 486

        (2012) 43–51. https://doi.org/10.1038/nature11115.

[5]   A. Coralli, B. Sarruf, P.E.V. de Miranda, L. Osmieri, S. Specchia, N.Q. Minh, Fuel cells, in:

        P.E.V. de Miranda (Ed.), Sci. Eng. Hydrog. Energy Technol., Elsevier Inc., 2019: pp. 39–

        122. https://doi.org/10.1016/B978-0-12-814251-6.00002-2.

[6]   H.A. Gasteiger, S.S. Kocha, B. Sompalli, F.T. Wagner, Activity benchmarks and

        requirements for Pt, Pt-alloy, and non-Pt oxygen reduction catalysts for PEMFCs, Appl.

        Catal. B Environ. 56 (2005) 9–35. https://doi.org/10.1016/j.apcatb.2004.06.021.

[7]   A. Casalegno, R. Marchesi, DMFC performance and methanol cross-over: Experimental

        analysis and model validation, J. Power SourcesValidation, DM. 185 (2008) 318–330.

        https://doi.org/https://doi.org/10.1016/j.jpowsour.2008.06.071.

[8]   C. Lo Vecchio, D. Sebastián, C. Alegre, A.S. Aricò, V. Baglio, Carbon-supported Pd and Pd-

        Co cathode catalysts for direct methanol fuel cells (DMFCs) operating with high methanol

        concentration, J. Electroanal. Chem. 808 (2018) 464–473.

        https://doi.org/https://doi.org/10.1016/j.jelechem.2017.02.042.

[9]   R. Escudero-Cid, P. Hernández-Fernández, J.C. Pérez-Flores, S. Rojas, S. Garcia-Rodríguez,

        E. Fatás, P. Ocón, Analysis of performance losses of direct methanol fuel cell with methanol

        tolerant PtCoRu/C cathode electrode, Int. J. Hydrogen Energy. 37 (2012) 7119–7130.

https://doi.org/10.1016/j.ijhydene.2011.12.158.

[10]   P. Stelmachowski, A.H.A. Monteverde Videla, K. Ciura, S. Specchia, Oxygen evolution
        catalysis in alkaline conditions over hard templated nickel-cobalt based spinel oxides, Int. J.
        Hydrogen Energy. 42 (2017) 27910–27918. https://doi.org/10.1016/j.ijhydene.2017.06.034.

[11]   H.S. Wroblowa, S.B. Qaderi, Mechanism and kinetics of oxygen reduction on steel, J.
        Electroanal. Chem. 279 (1990) 231–242. https://doi.org/10.1016/0022-0728(90)85179-9.

[12]   F. Jaouen, D. Jones, N. Coutard, V. Artero, P. Strasser, A. Kucernak, Toward platinum group
        metal-free catalysts for hydrogen/air proton-exchange membrane fuel cells, Johnson Matthey
        Technol. Rev. 62 (2018) 231–255. https://doi.org/10.1595/205651318X696828.

[13]   T. Asset, P. Atanassov, Iron-Nitrogen-Carbon Catalysts for Proton Exchange Membrane Fuel
        Cells, Joule. 4 (2020) 33–44. https://doi.org/10.1016/j.joule.2019.12.002.

[14]   S. Specchia, P. Atanassov, J.H. Zagal, Mapping transition metal–nitrogen–carbon catalyst
        performance on the critical descriptor diagram, Curr. Opin. Electrochem. 27 (2021) 100687.
        https://doi.org/10.1016/j.coelec.2021.100687.

[15]   S.T. Thompson, A.R. Wilson, P. Zelenay, D.J. Myers, K.L. More, K.C. Neyerlin, D.
        Papageorgopoulos, ElectroCat: DOE's approach to PGM-free catalyst and electrode R&D,
        Solid State Ionics. 319 (2018) 68–76. https://doi.org/10.1016/j.ssi.2018.01.030.

[16]   Y. Shao, J.P. Dodelet, G. Wu, P. Zelenay, PGM-Free Cathode Catalysts for PEM Fuel Cells:
        A Mini-Review on Stability Challenges, Adv. Mater. 31 (2019) 1–8.
        https://doi.org/10.1002/adma.201807615.

[17]   L. Osmieri, J. Park, D.A. Cullen, P. Zelenay, D.J. Myers, K.C. Neyerlin, Status and
        challenges for the application of platinum group metal-free catalysts in proton-exchange
        membrane fuel cells, Curr. Opin. Electrochem. 25 (2021) 100627.

https://doi.org/10.1016/j.coelec.2020.08.009.

[18] S. Rojas-Carbonell, K. Artyushkova, A. Serov, C. Santoro, I. Matanovic, P. Atanassov, Effect of pH on the Activity of Platinum Group Metal-Free Catalysts in Oxygen Reduction Reaction, ACS Catal. 8 (2018) 3041–3053. https://doi.org/10.1021/acscatal.7b03991.

[19] I. Matanovic, K. Artyushkova, P. Atanassov, Understanding PGM-free catalysts by linking density functional theory calculations and structural analysis: Perspectives and challenges, Curr. Opin. Electrochem. 9 (2018) 137–144. https://doi.org/10.1016/j.coelec.2018.03.009.

[20] W. Wang, Q. Jia, S. Mukerjee, S. Chen, Recent Insights into the Oxygen-Reduction Electrocatalysis of Fe/N/C Materials, ACS Catal. 9 (2019) 10126–10141. https://doi.org/10.1021/acscatal.9b02583.

[21] K. Artyushkova, A. Serov, S. Rojas-Carbonell, P. Atanassov, Chemistry of Multitudinous Active Sites for Oxygen Reduction Reaction in Transition Metal-Nitrogen-Carbon Electrocatalysts, J. Phys. Chem. C. 119 (2015) 25917–25928. https://doi.org/10.1021/acs.jpcc.5b07653.

[22] C.H. Choi, W.S. Choi, O. Kasian, A.K. Mechler, M.T. Sougrati, S. Brüller, K. Strickland, Q. Jia, S. Mukerjee, K.J.J. Mayrhofer, F. Jaouen, Unraveling the Nature of Sites Active toward Hydrogen Peroxide Reduction in Fe-N-C Catalysts, Angew. Chemie - Int. Ed. 56 (2017) 8809–8812. https://doi.org/10.1002/anie.201704356.

[23] S. Gottesfeld, D.R. Dekel, M. Page, C. Bae, Y. Yan, P. Zelenay, Y.S. Kim, Anion exchange membrane fuel cells: Current status and remaining challenges, J. Power Sources. 375 (2018) 170–184. https://doi.org/10.1016/j.jpowsour.2017.08.010.

[24] G. Merle, M. Wessling, K. Nijmeijer, Anion exchange membranes for alkaline fuel cells: A review, J. Memb. Sci. 377 (2011) 1–35. https://doi.org/10.1016/j.memsci.2011.04.043.

[25] S. Ratso, A. Zitolo, M. Käärik, M. Merisalu, A. Kikas, V. Kisand, M. Rähn, P. Paiste, J. Leis, V. Sammelselg, S. Holdcroft, F. Jaouen, K. Tammeveski, Non-precious metal cathodes for anion exchange membrane fuel cells from ball-milled iron and nitrogen doped carbide-derived carbons, Renew. Energy. 167 (2021) 800–810. https://doi.org/10.1016/j.renene.2020.11.154.

[26] M. Borghei, J. Lehtonen, L. Liu, O.J. Rojas, Advanced Biomass-Derived Electrocatalysts for the Oxygen Reduction Reaction, Adv. Mater. 30 (2018) 1–27. https://doi.org/10.1002/adma.201703691.

[27] J. Deng, M. Li, Y. Wang, Biomass-derived carbon: Synthesis and applications in energy storage and conversion, Green Chem. 18 (2016) 4824–4854. https://doi.org/10.1039/c6gc01172a.

[28] S. Tabac, D. Eisenberg, Pyrolyze this paper: Can biomass become a source for precise carbon electrodes?, Curr. Opin. Electrochem. 25 (2021) 100638. https://doi.org/10.1016/j.coelec.2020.09.005.

[29] P. Kaur, G. Verma, S.S. Sekhon, Biomass derived hierarchical porous carbon materials as oxygen reduction reaction electrocatalysts in fuel cells, Prog. Mater. Sci. 102 (2019) 1–71. https://doi.org/10.1016/j.pmatsci.2018.12.002.

[30] K.W. Chew, S.R. Chia, W.Y. Chia, W.Y. Cheah, H.S.H. Munawaroh, W.J. Ong, Abatement of hazardous materials and biomass waste via pyrolysis and co-pyrolysis for environmental sustainability and circular economy, Environ. Pollut. 278 (2021) 116836. https://doi.org/10.1016/j.envpol.2021.116836.

[31] A. Jain, S. Sarsaiya, M. Kumar Awasthi, R. Singh, R. Rajput, U.C. Mishra, J. Chen, J. Shi, Bioenergy and bio-products from bio-waste and its associated modern circular economy: Current research trends, challenges, and future outlooks, Fuel. 307 (2022) 121859.

https://doi.org/10.1016/j.fuel.2021.121859.

[32] M. Borghei, N. Laocharoen, E. Kibena-Põldsepp, L.S. Johansson, J. Campbell, E. Kauppinen, K. Tammeveski, O.J. Rojas, Porous N,P-doped carbon from coconut shells with high electrocatalytic activity for oxygen reduction: Alternative to Pt-C for alkaline fuel cells, Appl. Catal. B Environ. 204 (2017) 394–402. https://doi.org/10.1016/j.apcatb.2016.11.029.

[33] H. Zhou, J. Zhang, J. Zhu, Z. Liu, C. Zhang, S. Mu, A self-template and KOH activation co-coupling strategy to synthesize ultrahigh surface area nitrogen-doped porous graphene for oxygen reduction, RSC Adv. 6 (2016) 73292–73300. https://doi.org/10.1039/c6ra16703a.

[34] H. Zhou, J. Zhang, I. Amiinu, C. Zhang, X. Liu, W. Tu, M. Pan, S. Mu, Transforming waste biomass with an intrinsically porous network structure into porous nitrogen-doped graphene for highly efficient oxygen reduction, Phys. Chem. Chem. Phys. 18 (2016) 10392–10399. https://doi.org/https://doi.org/10.1039/C6CP00174B.

[35] Z. Zhang, S. Yang, H. Li, Y. Zan, X. Li, Y. Zhu, M. Dou, F. Wang, Sustainable Carbonaceous Materials Derived from Biomass as Metal-Free Electrocatalysts, Adv. Mater. 31 (2019) 1–16. https://doi.org/10.1002/adma.201805718.

[36] L. Wang, Z. Sofer, M. Pumera, Will Any Crap We Put into Graphene Increase Its Electrocatalytic Effect?, ACS Nano. 14 (2020) 21–25. https://doi.org/10.1021/acsnano.9b00184.

[37] N.K. Chaudhari, M.Y. Song, J.S. Yu, Heteroatom-doped highly porous carbon from human urine, Sci. Rep. 4 (2014) 1–10. https://doi.org/10.1038/srep05221.

[38] K.B. Ansari, S.Z. Hassan, R. Bhoi, E. Ahmad, Co-pyrolysis of biomass and plastic wastes: A review on reactants synergy, catalyst impact, process parameter, hydrocarbon fuel potential, COVID-19, J. Environ. Chem. Eng. 9 (2021) 106436. https://doi.org/10.1016/j.jece.2021.106436.

[39] M. Muhyuddin, J. Filippi, L. Zoia, S. Bonizzoni, R. Lorenzi, E. Berretti, L. Capozzoli, M. Bellini, C. Ferrara, A. Lavacchi, C. Santoro, Waste Face Surgical Mask Transformation into Crude Oil and Nanostructured Electrocatalysts for Fuel Cells and Electrolyzers, ChemSusChem. (2021) 1–15. https://doi.org/10.1002/cssc.202102351.

[40] C.O. Tuck, E. Pérez, I.T. Horvath, R.A. Sheldon, M. Poliakoff, Valorization of biomass: Deriving more value from waste, Science (80-.). 337 (2012) 695–699. https://doi.org/10.1126/science.1218930.

[41] N. Tripathi, C.D. Hills, R.S. Singh, C.J. Atkinson, Biomass waste utilisation in low-carbon products: harnessing a major potential resource, Npj Clim. Atmos. Sci. 2 (2019). https://doi.org/10.1038/s41612-019-0093-5.

[42] L. Osmieri, R. Escudero-Cid, M. Armandi, P. Ocón, A.H.A. Monteverde Videla, S. Specchia, Effects of using two transition metals in the synthesis of non-noble electrocatalysts for oxygen reduction reaction in direct methanol fuel cell, Electrochim. Acta. 266 (2018) 220–232. https://doi.org/10.1016/j.electacta.2018.02.036.

[43] L. Osmieri, R. Escudero-Cid, A.H.A. Monteverde Videla, P. Ocón, S. Specchia, Performance of a Fe-N-C catalyst for the oxygen reduction reaction in direct methanol fuel cell: Cathode formulation optimization and short-term durability, Appl. Catal. B Environ. 201 (2017) 253–265. https://doi.org/10.1016/j.apcatb.2016.08.043.

[44] A.H.A. Monteverde Videla, L. Osmieri, S. Specchia, Non-noble metal (NNM) catalysts for fuel cells: Tuning the activity by a rational step-by-step single variable evolution, in: J.H. Zagal, B. Fethi (Eds.), Electrochem. N4 Macrocycl. Met. Complexes Vol. 1 Energy, Second Ed., 2nd ed., Springer Nature, Switzerland, 2016: pp. 69–102. https://doi.org/10.1007/978-3-319-31172-2_3.

[45] M.A. Costa de Oliveira, P.P. Machado Pico, W. da S. Freitas, A. D'Epifanio, B. Mecheri,

Iron-based electrocatalysts for energy conversion: Effect of ball milling on oxygen reduction activity, Appl. Sci. 10 (2020). https://doi.org/10.3390/APP10155278.

[46] R. Schmidt, H. Martin Scholze, A. Stolle, Temperature progression in a mixer ball mill, Int. J. Ind. Chem. 7 (2016) 181–186. https://doi.org/10.1007/s40090-016-0078-8.

[47] L. Takacs, J.S. McHenry, Temperature of the milling balls in shaker and planetary mills, J. Mater. Sci. 41 (2006) 5246–5249. https://doi.org/10.1007/s10853-006-0312-4.

[48] Y.S. Kwon, K.B. Gerasimov, S.K. Yoon, Ball temperatures during mechanical alloying in planetary mills, J. Alloys Compd. 346 (2002) 276–281. https://doi.org/10.1016/S0925-8388(02)00512-1.

[49] M.C. Denis, P. Gouerec, D. Guay, J.P. Dodelet, G. Lalande, R. Schulz, Improvement of the high energy ball-milling preparation procedure of CO tolerant Pt and Ru containing catalysts for polymer electrolyte fuel cells, J. Appl. Electrochem. 30 (2000) 1243–1253. https://doi.org/10.1023/A:1026542821607.

[50] Z. Guo, Z. Xiao, G. Ren, G. Xiao, Y. Zhu, L. Dai, L. Jiang, Natural tea-leaf-derived, ternary-doped 3D porous carbon as a high-performance electrocatalyst for the oxygen reduction reaction, Nano Res. 9 (2016) 1244–1255. https://doi.org/10.1007/s12274-016-1020-2.

[51] D. Wu, Y. Shi, H. Jing, X. Wang, X. Song, D. Si, S. Liang, C. Hao, Tea-leaf-residual derived electrocatalyst: Hierarchical pore structure and self nitrogen and fluorine co-doping for efficient oxygen reduction reaction, Int. J. Hydrogen Energy. 43 (2018) 19492–19499. https://doi.org/10.1016/j.ijhydene.2018.08.201.

[52] James Sherwood, The significance of biomass in a circular economy, Bioresour. Technol. 300 (2020) 122755. https://doi.org/10.1016/j.biortech.2020.122755.

[53] A. Noori, M. Bartoli, A. Frache, E. Piatti, M. Giorcelli, A. Tagliaferro, Development of

pressure-responsive polypropylene and biochar-based materials, Micromachines. 11 (2020) 1–12. https://doi.org/10.3390/MI11040339.

[54] M. Giorcelli, M. Bartoli, A. Sanginario, E. Padovano, C. Rosso, M. Rovere, A. Tagliaferro, High-Temperature Annealed Biochar as a Conductive Filler for the Production of Piezoresistive Materials for Energy Conversion Application, ACS Appl. Electron. Mater. 3 (2021) 838–844. https://doi.org/10.1021/acsaelm.0c00971.

[55] A. Tagliaferro, M. Rovere, E. Padovano, M. Bartoli, M. Giorcelli, Introducing the novel mixed gaussian-lorentzian lineshape in the analysis of the raman signal of biochar, Nanomaterials. 10 (2020) 1–19. https://doi.org/10.3390/nano10091748.

[56] Y. Garsany, O.A. Baturina, K.E. Swider-Lyons, S.S. Kocha, Experimental methods for quantifying the activity of platinum electrocatalysts for the oxygen reduction reaction, Anal. Chem. 82 (2010) 6321–6328. https://doi.org/10.1021/ac100306c.

[57] G. Wu, K.L. More, C.M. Johnston, P. Zelenay, High-Performance Electrocatalysts for Oxygen Reduction Derived from Polyaniline, Iron, and Cobalt, (2011) 443–448.

[58] Y.C. Wu, D. Feng, W.F. Koch, Evaluation of liquid junction potentials and determination of pH values of strong acids at moderate ionic strengths, J. Solution Chem. 18 (1989) 641–649. https://doi.org/10.1007/BF00651000.

[59] A. Ohma, K. Shinohara, A. Iiyama, T. Yoshida, A. Daimaru, Membrane and Catalyst Performance Targets for Automotive Fuel Cells by FCCJ Membrane, Catalyst, MEA WG, ECS Trans. 41 (2019) 775–784. https://doi.org/10.1149/1.3635611.

[60] I. Martinaiou, A.H.A. Monteverde Videla, N. Weidler, M. Kübler, W.D.Z. Wallace, S. Paul, S. Wagner, A. Shahraei, R.W. Stark, S. Specchia, U.I. Kramm, Activity and degradation study of an Fe-N-C catalyst for ORR in Direct Methanol Fuel Cell (DMFC), Appl. Catal. B Environ. 262 (2020) 118217. https://doi.org/10.1016/j.apcatb.2019.118217.

[61]   D. Torsello, G. Ghigo, M. Giorcelli, M. Bartoli, M. Rovere, A. Tagliaferro, Tuning the microwave electromagnetic properties of biochar-based composites by annealing, Carbon Trends. 4 (2021) 100062. https://doi.org/10.1016/j.cartre.2021.100062.

[62]   P. Savi, M. Yasir, M. Bartoli, M. Giorcelli, M. Longo, Electrical and microwave characterization of thermal annealed sewage sludge derived biochar composites, Appl. Sci. 10 (2020). https://doi.org/10.3390/app10041334.

[63]   M. Bartoli, M.A. Nasir, P. Jagdale, E. Passaglia, R. Spiniello, C. Rosso, M. Giorcelli, M. Rovere, A. Tagliaferro, Influence of pyrolytic thermal history on olive pruning biochar and related epoxy composites mechanical properties, J. Compos. Mater. 54 (2020) 1863–1873. https://doi.org/10.1177/0021998319888734.

[64]   M. Bartoli, M. Giorcelli, P. Jagdale, M. Rovere, A. Tagliaferro, M. Chae, D.C. Bressler, Shape tunability of carbonized cellulose nanocrystals, SN Appl. Sci. 1 (2019) 1–15. https://doi.org/10.1007/s42452-019-1727-2.

[65]   M. Coleman, R. Gesch, A. Jaradat, R. Mitchell, D. Reicosky, Biomass-Bioenergy Crops in the United States: A Changing Paradigm, Am. J. Plant Sci. Biotechnol. 1 (2007).

[66]   Y. Gao, Q. Yue, B. Gao, A. Li, Insight into activated carbon from different kinds of chemical activating agents: A review, Sci. Total Environ. 746 (2020) 141094. https://doi.org/10.1016/j.scitotenv.2020.141094.

[67]   S. Bashkova, T.J. Bandosz, The effects of urea modification and heat treatment on the process of NO2 removal by wood-based activated carbon, J. Colloid Interface Sci. 333 (2009) 97–103. https://doi.org/10.1016/j.jcis.2009.01.052.

[68]   X. Yang, I.K.M. Yu, D.C.W. Tsang, V.L. Budarin, J.H. Clark, K.C.W. Wu, A.C.K. Yip, B. Gao, S.S. Lam, Y.S. Ok, Ball-milled, solvent-free Sn-functionalisation of wood waste biochar for sugar conversion in food waste valorisation, J. Clean. Prod. 268 (2020) 122300.

https://doi.org/10.1016/j.jclepro.2020.122300.

[69] M.L. Sekirifa, M. Hadj-Mahammed, S. Pallier, L. Baameur, D. Richard, A.H. Al-Dujaili, Preparation and characterization of an activated carbon from a date stones variety by physical activation with carbon dioxide, J. Anal. Appl. Pyrolysis. 99 (2013) 155–160. https://doi.org/10.1016/j.jaap.2012.10.007.

[70] M. Thommes, K. Kaneko, A.V. Neimark, J.P. Olivier, F. Rodriguez-Reinoso, J. Rouquerol, K.S.W. Sing, Physisorption of gases, with special reference to the evaluation of surface area and pore size distribution (IUPAC Technical Report), Pure Appl. Chem. 87 (2015) 1051–1069. https://doi.org/10.1515/pac-2014-1117.

[71] H. Hermann, T. Schubert, W. Gruner, N. Mattern, Structure and chemical reactivity of ball-milled graphite, Nanostructured Mater. 8 (1997) 215–229. https://doi.org/10.1016/S0965-9773(97)00010-X.

[72] Z.Y. Liu, S.J. Xu, B.L. Xiao, P. Xue, W.G. Wang, Z.Y. Ma, Effect of ball-milling time on mechanical properties of carbon nanotubes reinforced aluminum matrix composites, Compos. Part A Appl. Sci. Manuf. 43 (2012) 2161–2168. https://doi.org/10.1016/j.compositesa.2012.07.026.

[73] T. Eguchi, Y. Kanamoto, M. Tomioka, D. Tashima, S. Kumagai, Effect of ball milling on the electrochemical performance of activated carbon with a very high specific surface area, Batteries. 6 (2020). https://doi.org/10.3390/batteries6020022.

[74] J.H. Zagal, F. Javier Recio, C.A. Gutierrez, C. Zuñiga, M.A. Páez, C.A. Caro, Towards a unified way of comparing the electrocatalytic activity MN4 macrocyclic metal catalysts for O2 reduction on the basis of the reversible potential of the reaction, Electrochem. Commun. 41 (2014) 24–26. https://doi.org/10.1016/j.elecom.2014.01.009.

[75] A. Alsudairi, J. Li, N. Ramaswamy, S. Mukerjee, K.M. Abraham, Q. Jia, Resolving the Iron

Phthalocyanine Redox Transitions for ORR Catalysis in Aqueous Media, J. Phys. Chem. Lett. 8 (2017) 2881–2886. https://doi.org/10.1021/acs.jpclett.7b01126.

[76]   L. Osmieri, R.K. Ahluwalia, X. Wang, H.T. Chung, X. Yin, A.J. Kropf, J. Park, D.A. Cullen, K.L. More, P. Zelenay, D.J. Myers, K.C. Neyerlin, Elucidation of Fe-N-C electrocatalyst active site functionality via in-situ X-ray absorption and operando determination of oxygen reduction reaction kinetics in a PEFC, Appl. Catal. B Environ. 257 (2019) 117929. https://doi.org/10.1016/j.apcatb.2019.117929.

[77]   D. Sebastián, A. Serov, K. Artyushkova, P. Atanassov, A.S. Aricò, V. Baglio, Performance, methanol tolerance and stability of Fe-aminobenzimidazole derived catalyst for direct methanol fuel cells, J. Power Sources. 319 (2016) 235–246. https://doi.org/10.1016/j.jpowsour.2016.04.067.

[78]   C.N. Barnakov, G.P. Khokhlova, A.N. Popova, S.A. Sozinov, Z.R. Ismagilov, XRD characterization of the structure of graphites and carbon materials obtained by the low-temperature graphitization of coal tar pitch, Eurasian Chem. J. 17 (2015) 87–93. https://doi.org/10.18321/ectj198.

[79]   G.F. Goya, Handling the particle size and distribution of Fe3O4 nanoparticles through ball milling, Solid State Commun. 130 (2004) 783–787. https://doi.org/10.1016/j.ssc.2004.04.012.

[80]   J. Weiss, H. Zhang, P. Zelenay, Recent progress in the durability of Fe-N-C oxygen reduction electrocatalysts for polymer electrolyte fuel cells, J. Electroanal. Chem. 875 (2020) 114696. https://doi.org/10.1016/j.jelechem.2020.114696.

[81]   K. Kumar, P. Gairola, M. Lions, N. Ranjbar-Sahraie, M. Mermoux, L. Dubau, A. Zitolo, F. Jaouen, F. Maillard, Physical and Chemical Considerations for Improving Catalytic Activity and Stability of Non-Precious-Metal Oxygen Reduction Reaction Catalysts, ACS Catal. 8

(2018) 11264–11276. https://doi.org/10.1021/acscatal.8b02934.